Investigation of the continuous-wave and pulsed operation of emerging thulium ion-doped laser media around 2000 nm and preparation of ZnS and ZnSe host materials

by

Suat İçli

A Dissertation Submitted to the
Graduate School of Sciences and Engineering
in Partial Fulfillment of the Requirements for
the Degree of

Master of Science

in

Physics

KOÇ ÜNİVERSİTESİ

July 25, 2023

Investigation of the continuous-wave and pulsed operation of emerging thulium ion-doped laser media around 2000 nm and preparation of ZnS and ZnSe host materials

Koç University

Graduate School of Sciences and Engineering

This is to certify that I have examined this copy of a master's thesis by

Suat İçli

and have found that it is complete and satisfactory in all respects,
and that any and all revisions required by the final
examining committee have been made.

Committee Members:

_____

Prof. Alphan Sennaroğlu (Advisor)

_____

Assoc. Prof. Umut Aydemir [Co-Advisor]

_____

Prof. Alpan Bek

_____

Prof. Özgür Müstecaplıoğlu

_____

Res. Assist. Prof. Yağız Morova

Date: _____

To my grandmother Vahide

ABSTRACT

Investigation of the continuous-wave and pulsed operation of emerging thulium ion-doped laser media around 2000 nm and preparation of ZnS and ZnSe host materials

Suat İçli

Master of Science in Physics

July 25, 2023

In recent years, there has been a significant development in thulium ion-doped solid-state gain media capable of generating tunable, coherent laser radiation near 2000 nm. These lasers can operate in continuous-wave (CW), pulsed, and mode-locked modes, and have found applications in various fields such as surgery, spectroscopy, and pumping of mid-infrared optical parametric oscillators.

This thesis focuses on successful demonstration of self-Q-switched (SQS) operation of a thulium- doped lutetia (Tm^{3+}:Lu_2O_3) ceramic laser operating near 2 μm. By optimizing the cavity focusing, SQS operation was achieved at different discrete curved mirror separations without the need of an external modulator. This resulted in the generation of 9.7 μs pulses at the wavelength of 2091 nm and at the repetition rate of 26.7 kHz with 632 mW of pump power at 776 nm. Moreover, a carefully designed resonator was employed to enable low-threshold CW operation with a lasing threshold pump power as low as 33 mW. The CW Tm^{3+}:Lu_2O_3 ceramic laser exhibited a wide tuning range between 2073 and 2235 nm. This novel achievement paves the way for the development of highly efficient and versatile laser systems in the mid-infrared spectral region.

This research also focuses on various synthesis methods for producing thulium ion-doped ZnSe and ZnS solid-state gain media. Currently, single crystal and ceramic laser hosts are manufactured using methods such as the Czochralski process, Floating Zone, and chemical vapor deposition, which are time-consuming, expensive, and involve the use of hazardous chemicals. Alternative methods, including chemical vapor transport (CVT), vertical Bridgman technique for growing single crystals, and

spark plasma sintering for producing polycrystalline sampless, have been explored. Herein, ZnSe crystals were successfully obtained from ball-milled powders using the Bridgman technique. The CVT method, by using prereacted powders, resulted in a relatively high optical transmission of up to 40% for a 1.8 mm thick sample. Additionally, we explored the potential of thulium doping through high-energy ball milling as a technique to synthesize gain media for these crystals.

ÖZETÇE

Gelişmekte olan tulyum iyon katkılı lazer ortamının 2000 nm civarında sürekli dalga ve darbeli çalışmasının araştırılması ve ZnS/ZnSe barındıran malzemelerin oluşturulması

Suat İçli

Fizik, Yüksek Lisans

25 Temmuz 2023

Son yıllarda, 2000 nm'ye yakın ayarlanabilir, koherent lazer radyasyonu üretebilen tulyum iyonu katkılı katı hal kazanç ortamında önemli bir gelişme olmuştur. Bu lazerler, sürekli dalga (CW), darbeli ve mod kilitli modlarda çalışabilir ve cerrahi, spektroskopi ve orta kızılötesi optik parametrik osilatörlerin pompalanması gibi çeşitli alanlarda uygulama bulmuştur.

Bu tez, 2 μm yakınında çalışan bir tulyum katkılı lutetia (Tm^{3+}:Lu_2O_3) seramik lazerin kendinden Q anahtarlamalı (SQS) çalışmasının başarılı bir şekilde gösterilmesine odaklanmaktadır. Boşluğa odaklanmayı optimize ederek, harici bir modülatöre ihtiyaç duymadan farklı ayrı kavisli ayna ayrımlarında SQS işlemi sağlandı. Bu, 2091 nm dalga boyunda ve 776 nm'de 632 mW pompa gücü ile 26,7 kHz tekrarlama hızında 9,7 μs darbelerin üretilmesiyle sonuçlandı. Ayrıca, 33 mW kadar düşük bir kalıcı eşik pompa gücü ile düşük eşikli CW çalışmasını sağlamak için dikkatle tasarlanmış bir rezonatör kullanıldı. CW Tm^{3+}:Lu_2O_3 seramik lazer, 2073 ve 2235 nm arasında geniş bir dalga boyu ayarlama aralığı sergiledi. Bu yeni başarı, orta kızılötesi spektral bölgede oldukça verimli ve çok yönlü lazer sistemlerinin geliştirilmesinin yolunu açıyor.

Bu araştırma aynı zamanda tulyum iyon katkılı ZnSe ve ZnS katı hal kazanç ortamı üretmek için sentez yöntemlerine odaklanmaktadır. Şu anda, tek kristal ve seramik lazer ortamları, Czochralski işlemi, Floating Zone ve kimyasal buhar biriktirme gibi zaman alıcı, pahalı ve tehlikeli kimyasalların kullanımını içeren yöntemler kullanılarak üretilmektedir. Kimyasal buhar aktarımı (CVT), tek kristaller için dikey Bridgman tekniği ve seramikler için kıvılcım plazma sinterleme gibi alternatif

yöntemler araştırılmıştır. Bu çalışmada, CVT yöntemi, bilyeli öğütülmüş tozlarla 1.8 mm kalınlığındaki bir numune için %40'a varan bir optik iletim sağlamıştır. Bridgman tekniği kullanılarak bilyeli öğütülmüş tozlardan ZnSe kristalleri elde edilmiştir. Ayrıca, yüksek enerjili bilyeli öğütme kullanan tulyum katkılanması da bu kazanç ortamlarını sentezlemek için potansiyel bir teknik olarak araştırıldı.

ACKNOWLEDGMENTS

Firstly, I would like to express my deepest gratitude to my advisors Alphan Sennaroğlu and Umut Aydemir. Their guidance, support, and expertise have been invaluable throughout my thesis journey. I am truly grateful for the opportunities they have provided me. I would also like to extend my thanks to my thesis committee members, who have been instrumental in shaping my academic and research development. I am particularly grateful to Alpan Bek for his exceptional teaching during my bachelor's studies and for inspiring my interest in photonics. I would like to acknowledge Özgür Müstecaplığlu for his mentorship and guidance, which have been instrumental in shaping my future research career. I am indebted to Yağız Morova for his teachings on laser construction, as well as his scientific collaboration. I am also thankful to Sefa Öztulum for his valuable contributions and collaborations.

I would like to express my appreciation to Müjde Yahyaoğlu for her assistance in answering my various questions at KUBAM. I would also like to thank Naeimeh Sadat Peighambardoust and Bengisu Yılmaz for their contributions in band gap measurements, Hadi Jahangiri for his contributions in photoluminescence measurements, Gülsu Şimşek Franci for her expertise in ICP-MS measurements, Barış Yağcı for his support and expertise in SEM measurements, Arda Baran Burçak for his assistance in lattice parameter refinements and general help, and Ali Arda Aydın for his expertise in etching. I am grateful to all the members of the Laser Research Laboratory and the Boron and Advanced Materials Application and Research Center for their contributions and collaborations. I would also like to express my gratitude to Şahin *amca* for sharing his insights and knowledge with me.

Lastly, I would like to express my heartfelt appreciation to my family. I would

like to dedicate my thesis to my grandmother, Vahide, for her unwavering support and the joy she brings to my life.

This thesis is supported by the Scientific and Technological Research Council of Turkey (TÜBİTAK) with Grant Number 120F324. I want to thank TÜBİTAK for financial support.

TABLE OF CONTENTS

LIST OF TABLES

LIST OF FIGURES

ABBREVIATIONS

CW	Continuous-wave
SQS	Self-Q-Switching
GSRA	Ground-state reabsorption
TDL	Time-dependent lensing
ESA	Excited-state absorption
PQS	Passive Q-Switching
SQSML	Self-Q-switched mode locking
N_i	Number of electrons per unite volume of state i
L_c	Cavity loss
T_{OC}	Output coupler transmission
d_g	Gain medium length
γ	differential gain coefficient
G	fractional power gain
CVT	Chemical Vapor Transport
CVD	Chemical Vapor Deposition
η	Slope efficiency
η_a	fractional pump absorption
Q	time-dependent fractional loss
f_{rep}	Repetition rate
τ_p	Pulse duration

Chapter 1

INTRODUCTION

In recent years, the development of continuous-wave (CW) and pulsed lasers operating near 2 μm has received a great deal of attention because of numerous potential applications in atmospheric sensing [Singh et al., 2015], medicine [Belyaev et al., 2016], and in the pumping of longer wavelength solid-state lasers [Antipov et al., 2015] as well as optical parametric oscillators [Kolker et al., 2019]. Among potential candidates, thulium ion Tm^{3+}-doped gain media can be readily used to generate coherent, tunable radiation near 2 μm and 2.3 μm based on the optical transitions $^3F_4 \rightarrow {}^3H_6$ and $^3H_4 \rightarrow {}^3H_5$, respectively. For example, Tm^{3+} ion-doped YLF [Canbaz et al., 2017] and YAP [Guillemot et al., 2019] crystal lasers have been demonstrated to work at 2 μm and 2.3 μm in various operation regimes such as active/passive Q-switching [Niu et al., 2021] and Kerr lens mode locking [Canbaz et al., 2017]. Among other potential hosts for the Tm^{3+} ion, Lu_2O_3, in crystal or ceramic form, possesses a number of advantages, including broad absorption and emission spectra when doped with Tm^{3+} [Koopmann et al., 2011b], a wide transparency window over the 0.22–8 μm range, and high thermal conductivity [Loiko et al., 2018, Liu et al., 2022]. Furthermore, since Tm^{3+} and Lu^{3+} ions have roughly equal masses and radii, doping of Lu_2O_3 with Tm^{3+} does not cause a significant decrease in the thermal conductivity of the host [Pirri et al., 2022]. Over the last decade, numerous studies have been performed to investigate the laser performance of both ceramic and single-crystal Tm^{3+}:Lu_2O_3 lasers [Koopmann et al., 2011b, Loiko et al., 2018, Pirri et al., 2022, Antipov et al., 2011, Baylam et al., 2018, Schmidt et al., 2012, Koopmann et al., 2011a, Antipov et al., 2016, Lagatsky et al., 2013, Suzuki et al., 2021, Vetrovec et al., 2018, Antipov et al., 2012, Antipov et al., 2021, Sun

et al., 2021, Zhang et al., 2021, Ivakin et al., 2013]. In particular, CW [Koopmann et al., 2011b, Loiko et al., 2018, Antipov et al., 2011, Baylam et al., 2018, Koopmann et al., 2011a, Antipov et al., 2016, Vetrovec et al., 2018], Q-switched [Antipov et al., 2016, Antipov et al., 2012, Antipov et al., 2021, Sun et al., 2021]], and mode-locked [Schmidt et al., 2012, Lagatsky et al., 2013, Suzuki et al., 2021] operations have been demonstrated by utilizing 0.8-μm [Koopmann et al., 2011b, Antipov et al., 2011], 1.2-μm [Baylam et al., 2018], and in-band (1.7 μm) pumping [Suzuki et al., 2021, Antipov et al., 2021, Sun et al., 2021, Zhang et al., 2021]. In CW operation, as high as 68% slope efficiency was achieved with respect to the absorbed pump power [Koopmann et al., 2011b], and tunability over the 1890-2120 nm wavelength range was obtained [Vetrovec et al., 2018]. Combining Lu_2O_3 and Sc_2O_3 hosts, Suzuki et al. further demonstrated tunability from 1874 nm to 2171 nm, which, to the best of our knowledge, corresponds to the furthest operation wavelength obtained to date for the ${}^3F_4 \rightarrow {}^3H_6$ transition of the Tm^{3+} ion-doped sesquioxides [Pirri et al., 2022, Suzuki et al., 2021].

Self-Q-switching (SQS) is an effective method for the generation of laser pulses without the need for an external modulator inside the resonator. It has been observed in bulk and fiber media doped with various laser-active ions. Some examples include Yb^{3+} [Wang et al., 2022], Tm^{3+} [Zu et al., 2020], and Ho^{3+} [Li et al., 2019] doped fibers, as well as Nd^{3+} [Lu et al., 2002] and Cr^{3+} [Beyatli et al., 2013] doped bulk media. In the particular case of Tm^{3+}-doped hosts, SQS has also been demonstrated in the Tm^{3+}-doped YLF [Zhang et al., 2018], LuAG [Beyatlı et al., 2020], YAG [Zhang et al., 2020a], and YAP [Kang et al., 2022, Razdobreev and Shestakov, 2006, Cai et al., 2015, Wu et al., 2015]. In studies related to SQS in Tm^{3+}-doped lasers, different mechanisms have been proposed to explain the origin of SQS, including ground-state reabsorption (GSRA) [Zhang et al., 2018, Kang et al., 2022], time-dependent lensing (TDL) [Beyatlı et al., 2020, Zhang et al., 2020a], excited-state absorption (ESA) [Razdobreev and Shestakov, 2006] and chaotic dynamics [Wu et al., 2015]. However, additional work is needed in developing a comprehensive model. The lack of a physical modulator inside the resonator permits relatively

low-loss operation, allowing SQS to generate a nanosecond pulse [Dong et al., 2002] with kW peak powers [Fedin et al., 2001]. Hence, SQS lasers might be used to obtain compact, easy-to-integrate, low-cost pulsed lasers. More recently, Liu et al. [Liu et al., 2016] achieved shorter pulses with SQS compared to passive Q switching (PQS), and 50 W supercontinuum generation has been achieved by He et al. [He et al., 2022] by using an SQS fiber laser. Zhang et al. [Zhang et al., 2022] demonstrated an SQS vortex laser. Also, Wang et al. [Wang et al., 2022] obtained picosecond pulses at GHz repetition rate by self Q-switched mode locking (SQSML) with a Nd:LGGG waveguide laser. Recent developments suggest that SQS is a promising methodology with room for further development.

Infrared (IR) region extends from 750 nm to 1000 μm and divided into five subcategories namely; near-infrared (NIR) from 0.75 μm to 1.4 μm, short-wavelength infrared (SWIR) from 1.4 μm to 3 μm, mid-wavelength infrared (MWIR) from 3 μm to 8 μm, long-wavelength infrared (LWIR) from 8 μm to 15 μm, and far infrared from 15 μm to 1000 μm. Because of its long wavelength and low dispersion, the LWIR region has key applications in night detection and thermal imaging, among others. Materials with outstanding mechanical and thermal qualities, as well as high transmission in LWIR, are thus required for these applications. ZnS and ZnSe are two noteworthy examples, both of which have high tranmission in LWIR.

Zinc sulfide (ZnS) is a wide band gap semiconductor that plays a crucial role in various technological applications, including LEDs [Hwang et al., 2005], displays [Zhang et al., 2020b], and gas sensors [Wang et al., 2012]. The synthesis of ZnS powders can be accomplished through several methods, such as chemical vapor deposition (CVD) [Liu et al., 2006], physical vapor deposition (PVD) [Velumani and Ascencio, 2004], sol-gel [Anila et al., 2015], co-precipitation [Iranmanesh et al., 2015], hydrothermal [Hoa et al., 2009], and high-energy ball-milling [Pathak et al., 2013]. Bulk synthesis techniques include CVD [McCloy et al., 2011], spark plasma sintering (SPS) [Chen et al., 2015], chemical vapor transport (CVT) [Lauck, 2010], and hot pressing (HP) [Chlique et al., 2011]. While CVD offers materials with superior

optical and mechanical qualities, it comes with the downside of using toxic gaseous compounds and being a highly expensive process. On the other hand, SPS and CVT methods provide relatively easier and more accessible alternatives for bulk synthesis of ZnS. In previous studies focused on ZnS fabrication using SPS, researchers have explored different temperature and pressure profiles to optimize the synthesis process. These variations enable the fine-tuning of material properties to meet specific application requirements. Although ZnS has exhibited low transmission in the visible and near-infrared (NIR) regions, notable progress has been made in LWIR with SPS. For instance, Khaled et al. achieved a significant transmission rate of 70% at 9 μm , expanding the potential of ZnS for applications in the mid-infrared range [Khaled et al., 2021]. Additionally, Kim et al. successfully obtained dense ceramics with remarkably short dwelling times as short as 5 minutes, highlighting advancements in the efficiency of the synthesis process [Kim et al., 2008]. To further enhance the properties of ZnS materials, researchers have explored the effects of sintering additives. Ahn et al. conducted studies using sintering additives such as LiF and CaF_2 to investigate their impact on densification during the SPS process [Ahn et al., 2018]. These investigations provide valuable insights into the role of additives in optimizing the structure and properties of ZnS ceramics.

In the CVT method, transport agents play a crucial role in facilitating the synthesis of ZnS. Researchers have explored different agents, such as Lauck et al. using iodine (I_2) [Lauck, 2010] and Noda et al. using ammonium chloride (NH_4Cl) [Noda et al., 1990]. These studies demonstrate the versatility of the CVT method in tailoring the growth conditions and properties of ZnS. Furthermore, Wu et al. demonstrated the successful doping of ZnS with nickel (Ni) using the CVT method [Wu et al., 1989]. The introduction of doping in ZnS enables the incorporation of desirable characteristics and facilitates the alteration of its electronic properties, thereby expanding its potential for a wide range of applications. Notably, the demonstration of ZnS lasers through the doping of Fe^{2+} [Firsov et al., 2015] and Cr^{2+} [Sorokina et al., 2002] showcases the successful utilization of this approach.

ZnSe, as one of the earliest discovered semiconductors, has found widespread applications in the fields of electronics and optoelectronics. Its versatile use extends to lasers [Voronov et al., 2008], LEDs [Gao et al., 2021], solar cells [Okereke and Ekpunobi, 2011], logic gates [Wherrett, 1991], and scintillators [Ryzhikov et al., 2001], making it an essential component in various technological advancements. Over time, several methods have been employed to obtain ZnSe nanstructures, including solid-state reaction [Pol et al., 2008], chemical vapor deposition (CVD) [Luo et al., 2021], co-precipitation [Ahamed et al., 2016], ball-milling [Li et al., 2008] , and the hydrothermal method [Jørgensen et al., 2008]. These techniques have proven effective in synthesizing ZnSe nanostructures, which exhibit unique properties and tailored characteristics. When it comes to obtaining bulk materials, different approaches have been utilized, such as SPS [Wei et al., 2017], CVT [Li and Jie, 2003], CVD [Krause et al., 1994], HP [Avetisov et al., 2018], and the Bridgman method [Wang et al., 2001]. The Bridgman method and the CVT offer relative simplicity compared to other methods and are commonly employed for growing single and polycrystalline ZnSe. Notably, Wang et al. successfully employed the Bridgman method to obtain twin-free, transparent single and polycrystalline ZnSe, demonstrating its effectiveness in producing high-quality crystals. Furthermore, the incorporation of additional elements such as Co [Mierczyk et al., 2002], Bi [Oh et al., 2004], and Te [Lee et al., 2008], as well as laser-active ions including Fe^{2+} [Frolov et al., 2013] and Cr^{2+} [Komar et al., 2009], through the process of doping has also been achieved using CVT and Bridgman methods.

In this thesis, the main focus is on exploring continuous-wave (CW) and pulsed thulium-doped Lu_2O_3 laser systems, as well as investigating thulium-doped ZnS and ZnSe host materials. The ultimate objective is to develop efficient and high-performance CW and pulsed Tm:ZnS and Tm:ZnSe lasers. The choice of Tm-doped ZnS and ZnSe as host materials is driven by their superior thermal conductivities and transparency characteristics. These features make them highly suitable for high-power laser applications and enable the development of lasers and optical parametric oscillators that operate in the mid-wave infrared (MWIR) region.

Chapter 2

LASER THEORY

2.1 Introduction

An electromagnetic wave is transported by quantized energy packets known as photons in the picture of a quantized atom and an electromagnetic wave, and the atom has quantized energy levels. Based on the laws of thermodynamics, electrons in the atom occupy these levels. There are three different kinds of interactions between the atom and the photon in this paradigm. The first is one is absorption as shown in the Figure 2.1a. Absorption is the process by which an electron is moved from a lower state to a higher one when the energy of the photon reaches the energy gap between the discrete energy levels. The promoted electron, or any other electron remaining in the higher state, might potentially move to the lower state. During this process, a photon with energy equivalent to the energy difference between the states involved in the transition is emitted. This process is called spontaneous emission and it is shown in the 2.1b. Einstein also envisioned an additional interaction, where an electron may be distorted by a photon and go into a lower state, producing two photons with identical characteristics as illustrated in the Figure 2.1c. Laser is based on the latter interaction and the term "laser" stands for light amplification by stimulated emission of radiation. It is composed of a resonator which provides the feedback mechanism, gain medium and excitation source. It is a device to produce identical photons with the same frequency and high levels of temporal and spatial coherence.

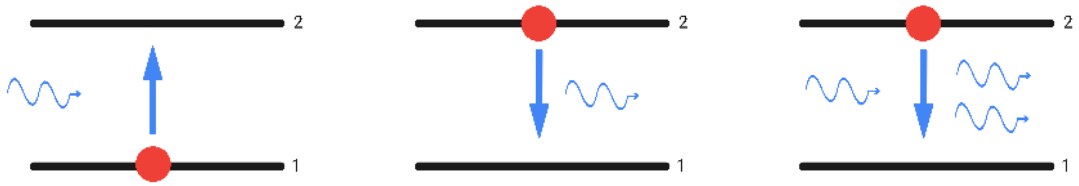

(a) (b) (c)

Figure 2.1: Light-matter interactions

2.2 Laser Dynamics

The population change of the upper energy state (N_2) of the gain medium can be determined by taking into account absorption, spontaneous emission, and stimulated emission processes. This is expressed by Equation 2.1, where energy levels and population are denoted as E_2, N_2, E_1, and N_1 for the upper and lower energy states, respectively.

$$\frac{dN_2}{dt} = \sigma_a \frac{I}{h\nu} N_1 - \frac{N_2}{\tau_f} - \sigma_e \frac{I}{h\nu} N_2 \tag{2.1}$$

In Equation 2.1, the first term corresponds to the population of electrons that are promoted to the upper state through absorption. The second and third terms represent the population of electrons that decay to the lower state through spontaneous emission and stimulated emission, respectively. Additionally, σ_a denotes the absorption cross section, I refers to the intensity of the incident field, h represents Planck's constant, ν represents the frequency of light, τ_f represents the fluorescent lifetime of the state, and σ_e represents the emission cross section, for further details see Chapter 6 of [Sennaroglu, 2010].

The laser operation can be understood by working out 2.1 starting from optical amplification. Assuming that a monochromatic light of frequency ν is incident on the gain medium, net difference between stimulated emission and absorption will contribute to the optical amplification. Since spontaneous emission happens

randomly in all directions, its effect can be disregarded. Additionally, the emission and absorption coefficients are assumed to be identical. Consequently, within an extremely small area of the gain medium, the intensity (I) will undergo a change as described in 2.2.

$$\frac{dI}{dz} = \sigma \Delta N I = \gamma(\nu) I \tag{2.2}$$

$\gamma(\nu)$ is the differential gain coefficient with dimensions inverse length, and $\Delta N = N_2 - N_1$. Optical amplification occurs when γ is greater than zero where $\Delta N > 0$, a condition known as population inversion. In the steady state $dN_2/dt = 0$, the populations between N_1 and N_2 have a relationship as in Equation 2.3. Since $N_1 > N_2$, population inversion is not possible for two level systems.

$$N_1 = \frac{\tau_f + 1}{\tau_f} N_2 \tag{2.3}$$

With a four-level system population inversion can be readily achieved. The energy level diagram for a four-level system is depicted in Figure 2.2. In the diagram, the blue arrows represent the processes involving absorption and emission of photons, while the orange arrows represent rapid non-radiative decay processes. Due to the quick decay from energy level 1, $\Delta N \approx N_2$. The corresponding rate equations for this system are given by Equation 2.4

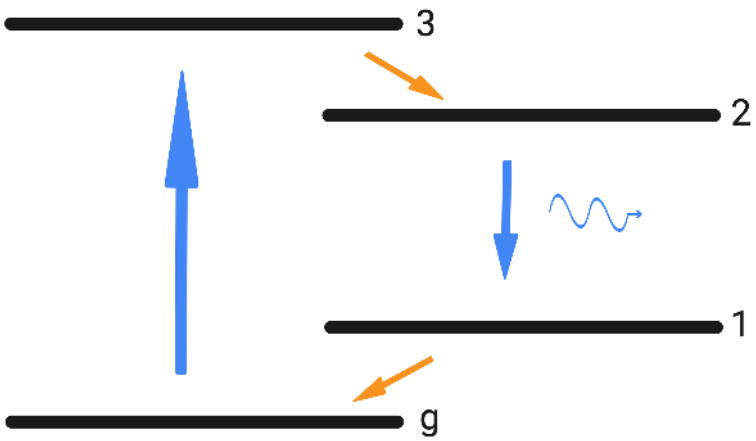

Figure 2.2: Energy level diagram of a four-level system. While blue arrows represent radiative processes, orange arrows represent fast non-radiative processes.

$$\frac{dN_2}{dt} = \sigma_a \frac{I_p}{h\nu_p} N_g - \frac{N_2}{\tau_f} - \sigma_e \frac{I_l}{h\nu_l} N_2 \tag{2.4}$$

At a steady state, the population inversion can be determined using Equation 2.5. As the intensity of the laser light increases, the population becomes saturated at a constant level. This saturation also affects the differential gain coefficient, γ, which is linked to the population inversion according to Equation 2.2. Consequently, the saturated differential gain coefficient can be expressed in relation to the unsaturated gain coefficient, γ_0, and the saturation intensity, I_{se}.

$$N_{2s} = \frac{\sigma_a I_p N_g \tau_f / h\nu_p}{1 + \dfrac{\sigma_e I_l \tau_f}{h\nu_l}} \tag{2.5}$$

$$\gamma = \frac{\gamma_0}{1 + \dfrac{I_l}{I_{se}}} \tag{2.6}$$

$$I_{se} = \frac{h\nu_l}{\sigma_e \tau_f} \tag{2.7}$$

$$\gamma_0 = \frac{\sigma_e \sigma_a I_p N_g \tau_f}{h\nu_p} \tag{2.8}$$

To maintain amplification, a resonator consisting of two mirrors is required. This cavity facilitates the amplification process, allowing the intensity to increase until lasing is achieved. The occurrence of lasing can be identified by observing the progression of light intensity within the cavity. Assuming that the total length of the amplifier is denoted as d_g, after each round trip, the intensity at the (m+1)th round trip can be described by Equation 2.9.

$$I_{m+1} = R_1 R_2 e^{(\gamma - \alpha) 2 d_g} I_m \tag{2.9}$$

There are two distinct regimes concerning the light intensity, denoted as I_l. The first regime is known as the small signal regime, where $\gamma = \gamma_0$. In this case, during

each round trip, the light intensity increases exponentially according to Equation 2.2. However, this exponential growth cannot continue indefinitely. As the light intensity, I_l, increases, the differential gain coefficient starts to decrease. When I_l reaches the saturation intensity, I_{se}, the differential gain coefficient becomes half of its unsaturated value. This is due to the increased loss of electrons from the population inversion (N_2) caused by stimulated emission. This limitation on the population inversion sets a threshold value, which corresponds to the point of lasing. The threshold differential gain coefficient can be calculated using Equation 2.9. During steady state or lasing operation, the light intensity remains constant ($I_{m+1} = I_m$). At the lasing or threshold point, both the differential gain coefficient and population inversion can be determined.

$$\gamma_{th} = \alpha + \frac{1}{2d_g} ln \left(\frac{1}{R_1 R_2} \right) \tag{2.10}$$

$$N_{2th} = \frac{\gamma_{th}}{\sigma_e} \tag{2.11}$$

Under the thin length approximation, the fractional power gain, denoted as G, is defined as the ratio of the change in laser light power to the laser light power itself as in Equation 2.12 [Sennaroglu, 2010], where the laser light power is $P_l = I_l a$, a is the area of the beam.

$$G = \frac{\Delta P_l}{P_l} \tag{2.12}$$

Then, $G = \sigma_e N_2 d_g$. Multiplying Equation 2.2 with $\sigma_e d_g$, rate equations in terms of G can be obtained as in 2.13 [Sennaroglu, 2010].

$$\frac{dG}{dt} = -\frac{G(t) - G_0}{\tau_f} - \frac{P_l(t) G(t)}{E_{sat}} \tag{2.13}$$

Saturation energy is defined as in 2.14

$$E_{sat} = \frac{h\nu_l}{\sigma_e} a \tag{2.14}$$

The small signal fractional gain is defined as shown in Equation 2.15.

$$G_0 = \frac{\sigma_a I_p N_t}{h\nu_p} \sigma_e d_g \tau_f \tag{2.15}$$

In this definition, there exists a linear relationship between the small signal gain and the pump intensity.

At the steady state, the rate of change of gain becomes zero, indicating a constant gain value. Equation 2.16 describes the steady state gain as a function of laser power.

$$G_s = G_{th} = \frac{G_0}{1 + \frac{P_l}{P_{sat}}} \tag{2.16}$$

where $P_{sat} = E_{sat}/\tau_f$.

By performing a similar derivation for $P_l(t)$, the time rate of change in laser power can be obtained, as shown in Equation 2.17. For further details, please refer to the [Sennaroglu, 2010]. By analyzing this equation in the steady-state case or continuous wave (CW) operation, the output power P_{out} can be calculated. Equation 2.18 demonstrates that this equation has a linear relationship with the pump power.

$$\frac{dP_L(t)}{dt} = -\frac{P_L(t)}{\tau_p} + 2\frac{G(t)}{T_R} P_L(t) \tag{2.17}$$

$$P_{out} = T_{OC} \frac{P_{sat}}{2} (\frac{G_0}{G_{th}} - 1) \tag{2.18}$$

Equation 2.18 can be alternatively expressed in terms of the pump power, P_p, and the threshold pump power, $(P_p)_{th}$, instead of fractional gain coefficients. The threshold pump power, $(P_p)_{th}$, can be calculated based on the cavity loss, L_c, and the output coupler transmission, T_{OC}, as illustrated in Equation 2.19. Moreover, by measuring the threshold pump power for various output couplers, the cavity loss can be easily determined.

$$(P_p)_{th} = A(L_c + T_{OC}) \tag{2.19}$$

The slope efficiency, denoted as η, is a significant parameter that quantifies the performance of a laser. It is defined as the ratio of the change in the output power

to the corresponding change in the input power. In other words, it represents the efficiency of converting input power into output power.

$$\eta = \frac{\Delta P_{out}}{\Delta P_p} \tag{2.20}$$

$$\eta = \frac{\lambda_p}{\lambda_l} \frac{T_{OC}}{T_{OC} + L_c} \eta_a \tag{2.21}$$

Fractional pump absorption, η_a is given by 2.22

$$\eta_a = \sigma_a N_g d_g = \sigma_a N_t d_g \tag{2.22}$$

Instead of Equation 2.18, the output power can be expressed in terms of the pump power and the threshold pump power. This formulation allows for a direct relationship between the output power and the pump power at or above the threshold level.

$$P_{out} = \eta(P_p - (P_p)_{th}) \tag{2.23}$$

When considering additional energy levels that affect the population inversion, a more accurate representation of laser operation can be achieved. One such scenario occurs when a laser photon is absorbed by an excited or ground-state electron, as depicted in Figure 2.3. Taking into account these additional levels and processes, such as ground-state absorption (GSRA) and excited-state absorption (ESA), the rate equations governing the population dynamics of the energy levels in the laser system need to be modified. Equation 2.24 presents the adjusted rate equation for the population of the upper energy level N_2.

$$\frac{dN_2}{dt} = \sigma_a \frac{I_p}{h\nu_p} N_g - \frac{N_2}{\tau_f} - \sigma_e \frac{I_L}{h\nu_L} N_2 - (\sigma_{esa})_p \frac{I_p}{h\nu_p} N_2 - (\sigma_{esa})_L \frac{I_L}{h\nu_L} N_2 \tag{2.24}$$

It incorporates various terms that contribute to the change in the population of N_2 over time. These terms include the absorption of pump light by electrons in the ground state ($\sigma_a I_p/(h\nu_p)N_g$), the decay of N_2 due to spontaneous emission (N_2/τ_f), the emission of N_2 caused by the laser light ($\sigma_e I_L/(h\nu_L)N_2$), as well as the

excited-state absorption processes for both pump light ($(\sigma_{esa})_p I_p/(h\nu_p)N_2$) and laser light ($(\sigma_{esa})_L I_L/(h\nu_L)N_2$) [Sennaroglu, 2019].

Indeed, the excited-state absorption cross sections, $(\sigma_{esa})_p$ and $(\sigma_{esa})_L$, quantify the probability of absorption taking place when the electrons are in the excited state. These processes play a significant role in reducing the population inversion by decreasing the populations of N_g and N_2. The reduction in the population inversion has significant implications for the performance and operation of the laser, as discussed in the introduction (refer to Chapter 1).

The inclusion of ground-state absorption (GSRA) and excited-state absorption (ESA) processes can result in pulsed operation of the laser, where the emission of light occurs in short pulses rather than a continuous output. These processes introduce additional dynamics and complexities into the laser system, which must be taken into account to achieve a comprehensive understanding of its behavior. The interplay between these processes, along with other factors such as gain saturation and cavity dynamics, can significantly influence the pulsing characteristics of the laser. Studying and analyzing these dynamics is crucial for a thorough comprehension of the laser's operation.

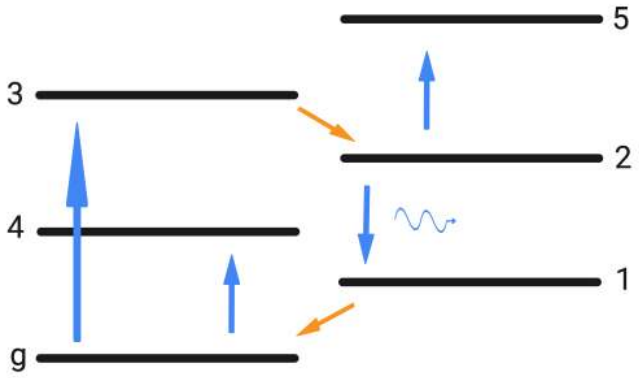

Figure 2.3: Modified four-level energy diagram which includes additional states 4 and 5.

2.3 Passive Q-Switching

Certainly, in addition to continuous wave (CW) operation, another important operating regime of lasers is q-switching. In q-switching, the laser emits pulses of light, and this can be achieved through active or passive means. Given the relevance to this thesis, only passive q-switching will be investigated from this point forward. In passive q-switching, a modulator based on the saturation effect is introduced into the laser cavity. This modulator, known as a saturable absorber, exhibits low absorption for intense laser pulses, allowing them to pass through while blocking other light. The internal dynamics of the saturable absorber are modulated rapidly enough to generate pulses with durations on the order of nanoseconds, as mentioned in Chapter 1. Passive q-switching provides a means to generate high-intensity laser pulses, which find applications in various fields such as materials processing, laser machining, and medical treatments. Understanding the internal dynamics and behavior of the saturable absorber is crucial for optimizing and controlling the q-switched laser pulses.

In the presence of a saturable absorber, a time-dependent fractional loss, denoted as Q, is introduced into the laser system. The rate of change of Q over time is governed by Equation 2.25. In this equation, τ_a represents the lifetime of the absorber atoms, Q_0 represents the small signal fractional loss, and E_a denotes the saturation energy of the absorber. The dynamics of Q play a crucial role in the performance and operation of the passive q-switched laser. By understanding and controlling the time-dependent behavior of the saturable absorber, one can manipulate the pulse characteristics and achieve desirable pulse durations and energy levels [Sennaroglu, 2010].

$$\frac{dQ}{dt} = -\frac{Q(t) - Q_0}{\tau_a} - \frac{P_l(t)Q(t)}{E_a} \tag{2.25}$$

$$\frac{dP_l}{dt} = \frac{2}{T_R}(G(t) - l - Q(t))P_l(t) \tag{2.26}$$

In Equation 2.26, $l = L_c/2$. Repetitive q-switching can be achieved if the condition specified in Equation 2.27 is satisfied. In this equation, T_f represents the ratio of the upper-state lifetime (τ_f) to the round-trip time (T_R) of the laser cavity. Additionally, P_a corresponds to the saturation energy (E_a) divided by the absorber's lifetime (τ_a). When the condition in Equation 2.27 holds true, the laser system is capable of producing repetitive q-switched pulses. The repetition rate of these pulses is linearly dependent on the pump power as shown in 2.29. By controlling the pump power, one can adjust the repetition rate of the q-switched laser output. This characteristic makes repetitive q-switching a valuable technique in various applications that require high-frequency pulsed laser output.

$$\frac{2Q_0T_f}{\chi} > 1 \tag{2.27}$$

$$\chi = \frac{P_a}{P_{sat}} \tag{2.28}$$

$$f_{rep} = \frac{1}{\tau_f}\frac{G_0}{2Q_0} \tag{2.29}$$

Chapter 3

CONTINUOUS-WAVE OPERATION OF THULIUM-DOPED LUTETIA LASER

3.1 Absorption and Output Characteristics

To pump the Tm^{3+}:Lu_2O_3 ceramic laser, a home-made 532 nm-pumped tunable Ti^{3+}:*Sapphire* laser was used. The details of the Ti^{3+}:*Sapphire* pump laser can be found in [Muti et al., 2019]. A half-wave plate (HWP) and a polarizing beam splitter (PBS) were further used to control the amount of incident pump power on the 2.76-mm-thick (effective length, d_g = 3 mm at Brewster's incidence), 1.5 at. % Tm^{3+}:Lu_2O_3 ceramic (Konoshima Chemicals Co., Japan, effective Tm^{3+} concentration: $N_t = 4.3 * 10^{20} cm^{-3}$). After the construction of the Ti^{3+}:Sapphire pump laser, the absorption characteristics of the ceramic were investigated by employing the open-aperture z-scan method [see Fig. 1(a)]. A converging lens (f = 5 cm) was used to focus the pump beam at the wavelength of 776 nm into the ceramic. In the air, the waists of the focused beam were measured with a beam profiler (Thorlabs BPM209) as 15 μm x 18 μm along the x- and y-axes, corresponding to root-mean-squared (RMS) values of 18 μm x 20 μm. Based on this measurement, the RMS beam area within the crystal was estimated as $2.24 * 10^{-4} cm^2$. As the ceramic sample was translated near the beam focus location, the maximum change in the power transmission was measured as 10%, bringing the overall power transmission to 74%, as shown in Fig. 1(b). By following the procedure described in [Morova et al., 2022], open aperture z-scan data displayed in Fig. 1(b) were analyzed and the saturation power, P_{sa}, was found as 1170 mW. The absorption cross-section, σ_a, at 776 nm was then determined as $1.52 * 10^{-21} cm^2$ by using

$$P_{sa} = \frac{hca_p}{\lambda_p \sigma_a \tau_f}. \tag{3.1}$$

In Equation 3.1, h is Planck's constant, c is the speed of light, a_p is the effective pump beam area, λ_p is the pump wavelength, and τ_f is the fluorescence lifetime. τ_f was assumed to be 3.22 ms [Eremeev et al., 2022]. Transmission of the gain medium was also recorded as a function of incident power at the focus location that gives the maximum absorption saturation (see 3.1b). Alternatively, P_{sa} could be obtained from the change in the transmission of the ceramic with respect to the incident pump power [see 3.1c]. In that case, P_{sa} was found as 1199 mW which gave $\sigma_a = 1.49x10^{-21}cm^2$ by using 3.1. The two σ_a values determined from the saturation analysis were comparable with each other and nearly two times lower than the reported values [Antipov et al., 2011] obtained at higher pumping wavelengths around 800 nm. Two curved mirrors (M1, M2, R=5 cm) and two flat mirrors (M3 (HR) and M4 (1% OC)) were used to complete the Tm^{3+}:Lu_2O_3 resonator, as shown in Figure 3.2a. To increase the pump absorption, another curved mirror (M5, R = 10 cm) highly reflective at the pump wavelength was inserted after M2. The laser cavity configuration was referred to as "single end-pumped" or "double end-pumped", depending on whether M5 was blocked or not. All mirrors used in the resonator had high reflective coatings in the 2100 - 2500 nm wavelength range. The total length of the resonator was 131 cm with the HR (length = 33 cm) and OC arms (length = 27 cm) folded by 17° and 13°, respectively. After the alignment of the Tm^{3+}:Lu_2O_3 resonator was optimized, CW lasing could be readily achieved at the free running wavelength of 2097 nm. The excitation spectrum given in Figure 3.2b shows the measured variation of the CW output power of the Tm^{3+}:Lu_2O_3 ceramic laser as a function of the pump wavelength at the constant incident pump power of 400 mW. According to our earlier transmission measurements (see [Baylam et al., 2018]), the pump absorption is maximum at 796 nm rather than at 776 nm. However, due to the tight focusing of the pump beam, higher absorption cross section at 796 nm also led to more absorption saturation, resulting in higher effective pump absorption at 776 nm. Hence, the wavelength of 776 nm was found to be more optimum for pumping the Tm^{3+}:Lu_2O_3 ceramic laser in this experiment, as can be

seen in 3.2b. Estimated slope efficiencies with respect to the incident pump power were 16% and 30%, and the threshold incident power for lasing was 50 mW and 33 mW, respectively, for single end-pumped and double end-pumped configurations, as shown in Figure 3.2c. As can be seen from the measured output spectrum shown in Figure 3.2d, the free-running output wavelength of the Tm^{3+}:Lu_2O_3 ceramic laser was 2097 nm.

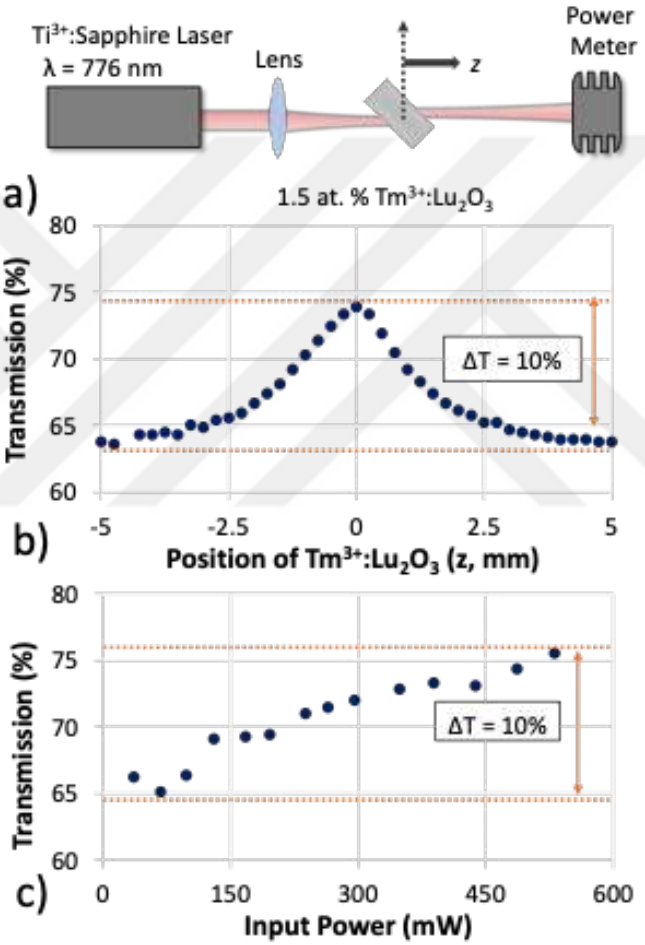

Figure 3.1: (a) Schematic of the experimental setup of the open aperture z-scan method used for absorption saturation measurements, (b) measured variation in the transmission as a function of the ceramic position at the incident pump power of 550 mW, and (c) measured variation in the transmission as a function of the input power for the case where the pump beam is focused near the center of the Tm^{3+}:Lu_2O_3 ceramic.

By using a beam profiler, the M^2 parameter was determined as 1.08 and 1.06 for the x and y directions, respectively, as shown in Figure 3.3 Based on the ABCD

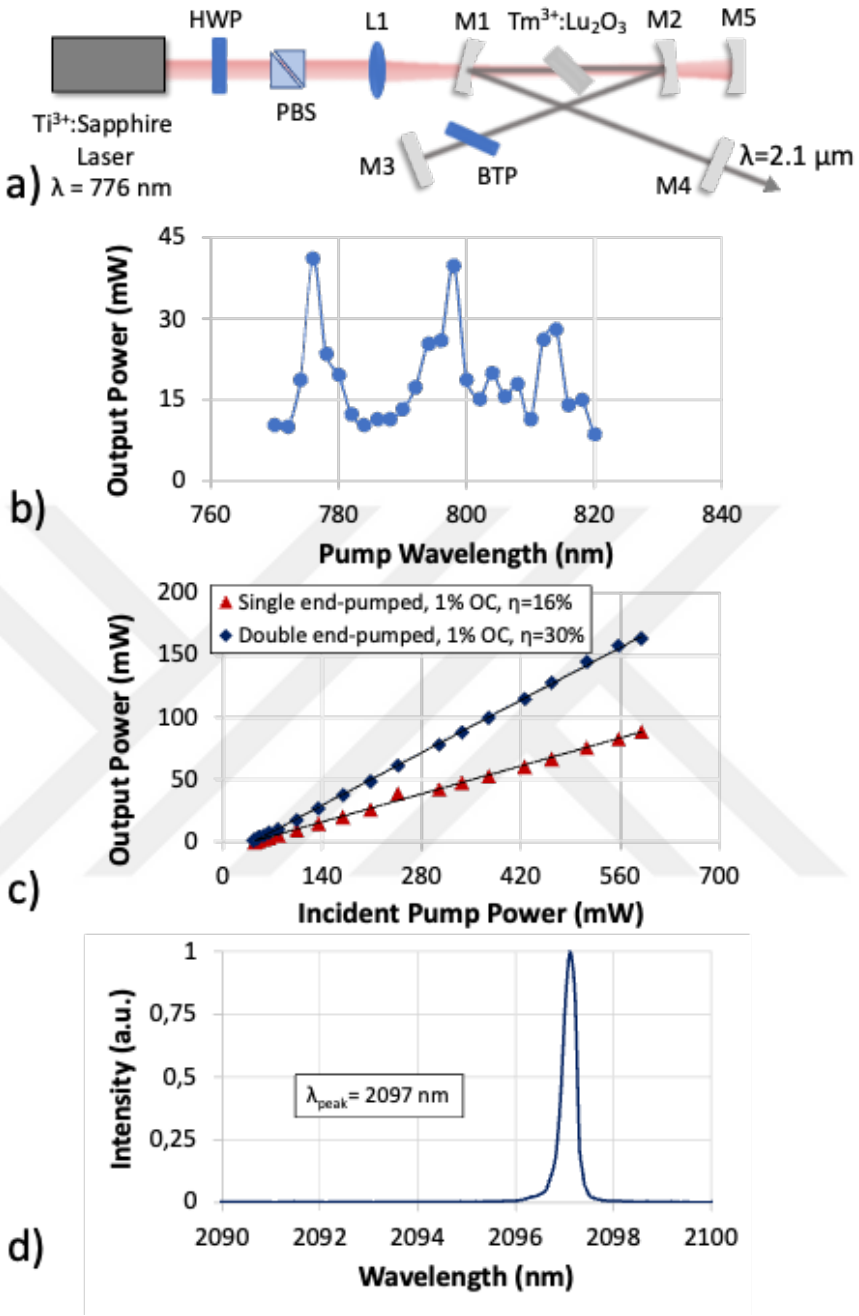

Figure 3.2: (a) Schematic of the experimental setup of the Tm^{3+}:Lu_2O_3 ceramic laser, (b) excitation spectrum of the Tm^{3+}:Lu_2O_3 laser showing the measured output power as a function of the pump wavelength at the constant incident pump power of 400 mW, (c) measured power efficiency curves for single end-pumped and double end-pumped configurations during CW operation, and (d) measured output spectrum of the free-running laser during CW operation.

analysis of the resonator, the RMS spot size of the focused laser beam inside the gain medium was estimated to be 41 μm. By using the power slope efficiency and the threshold data, the gain cross-section,σ_e, was further determined (See [Morova et al., 2022] for the details) as $0.81x10^{-21}cm^2$ at 2097 nm from the equation.

$$\sigma_e = \eta_o \frac{\pi}{4} \frac{hc}{\lambda_l} \frac{T_{OC}}{(P_a)_{th}\eta\tau_f} n({w_p}^2 + {w_l}^2) \tag{3.2}$$

In Equation 3.2, η_o (58%) is the estimated overlap factor of the laser and pump spot sizes, λ_l is the laser wavelength, T_{OC} (1%) is the output coupler transmission, n is the refractive index of the gain medium, η is the slope efficiency with respect to the absorbed power, $(P_a)_{th}$ is the threshold absorbed pump power, w_p (19 µm) and w_l (41 µm) are the pump and laser RMS spot sizes, respectively. η and $(P_a)_{th}$ were determined as 45% and 18 mW, respectively from the power efficiency curve (See Figure 3.2c) and threshold data.

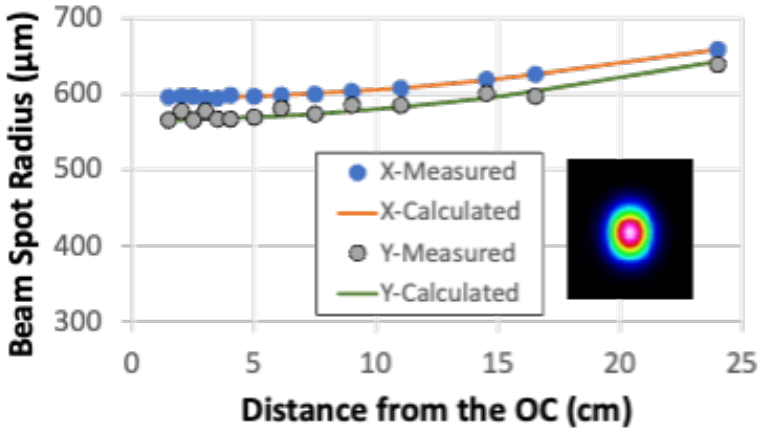

Figure 3.3: Experimental and calculated variation of the beam spot size as a function of distance from the output coupler (OC). The M^2 parameter was calculated as 1.08 and 1.06 for x and y directions, respectively. The inset shows the measured output beam intensity profile.

3.2 Tunability of CW Tm^{3+}:Lu_2O_3

To investigate the tunability of the laser, a 3-mm-thick birefringent tuning plate (BTP in Figure 3.2a) was inserted at Brewster incidence in the HR arm, and tunability was recorded with a scanning spectrometer (APE Wavescan). As shown in Figure 3.2d, the laser operated at the free-running wavelength of 2097 nm with a linewidth (FWHM) of 0.3 nm. Near the wavelength of 2066 nm, HR transmission reached 80% (Figure 3.4), which prohibited tunability below 2070 nm. Note that with mirrors having high reflectivity in the 2000 - 2100 nm range, the free running wavelength would have been close to the peak emission wavelength of 2066 nm [Loiko et al., 2018]. In our experiments, at the highest available incident power of 1W, tunability between 2075 - 2192 nm and 2073 - 2235 nm have been obtained for single end-pumped and double end-pumped configurations, respectively, as shown in Figure 3.5. The wavelength of 2235 nm, demonstrated in this study, is the longest operation wavelength of Tm-doped sesquioxide lasers, to the best of our knowledge.

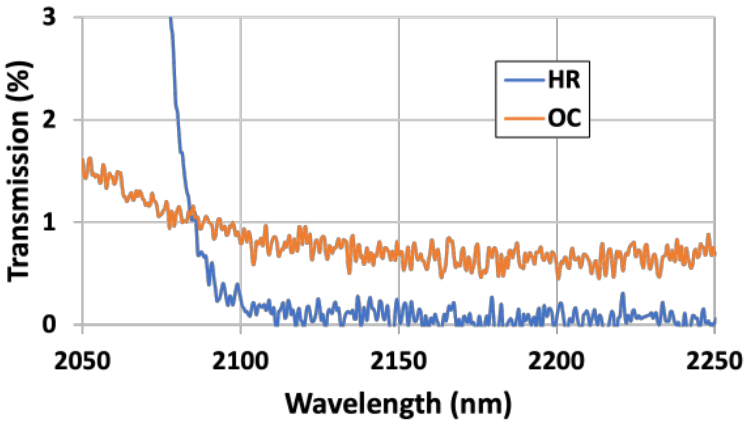

Figure 3.4: Transmission curves of OC and HR around the tuning region of the laser (2050-2250 nm)

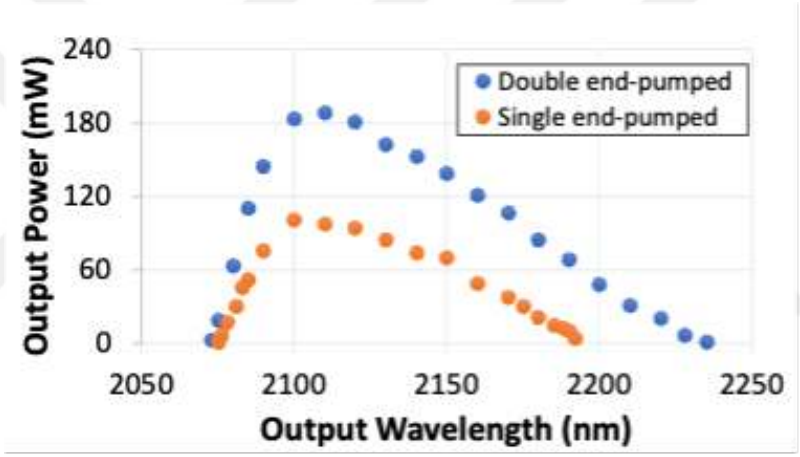

Figure 3.5: Tuning curves of the Tm^{3+}:Lu_2O_3 ceramic laser for single end-pumped and double end-pumped configurations during CW operation at the incident pump power of 1W.

Chapter 4

SELF-Q-SWITCHED OPERATION OF THULIUM-DOPED LUTETIA LASER

4.1 SQS Characteristics and Analysis

Following the CW characterization, BTP was removed from the cavity and SQS operation was investigated near the free running wavelength. In our experiments, the most critical parameter for initiating SQS operation was the separation between curved mirrors M1 and M2 shown in Figure 3.2a. In particular, to change the M1-M2 separation, M2 was mounted on a translation stage. As the mirror M2 was moved, the temporal output behavior was monitored with a photodetector connected to an oscilloscope (Tektronix TDS-2012B). At several discrete M1-M2 separations, pulsing was observed in a repeatable fashion. SQS operation was observed for both single end-pumped and double end-pumped configurations. Because the pulsed operation was more stable in single end-pumped configuration, experimental characterization of SQS operation was performed for this case only. The output power for CW and SQS operations was recorded as a function of the M1-M2 separation as shown in Figure 4.1(a). The pulse train was sensitive to position changes comparable to the minimum resolvable step of 10 μm of the translation stage. At a separation of 66.04 mm and with 632 mW of incident power the pulse train and the single pulse profile shown in Figures 4.1b and 4.1c were recorded for the single end-pumped configuration. At this separation, the laser beam waist in the gain medium was calculated as 26 μm, corresponding to an RMS value of 29 μm, while the pump beam waist remained approximately the same at 19 μm. As the incident power was increased, the peak power and the repetition rate also increased. In addition, the pulse width decreased, as shown in Figure 4.2b. Stable pulse train was obtained at incident pump powers above 360 mW. At 632 mW of incident power, SQS produced

9.7 μs wide pulses at the pulse repetition frequency of 26.7 kHz, with an output power of 17 mW. The corresponding average energy and peak power were determined as 0.63 μJ and 65 mW, respectively. Up to the maximum pump power of 632 mW investigated during pulsing experiments, we observed SQS operation with no saturation of peak power as can be seen in Figure 4.2b. To have better insight into the SQS operation, it was analyzed with a simple passive Q switching model as described in [Beyatli et al., 2013]. According to this model, the repetition rate can be expressed in terms of the small-signal loss Q_0 as

$$f_{rep} = \frac{1}{\tau_f}\frac{G_0}{2Q_0} \tag{4.1}$$

where G_0 is the round-trip small signal power gain which can be calculated from

$$P_{out} = T_{OC}\frac{P_{sat}}{2}(\frac{G_0}{G_{th}} - 1) \tag{4.2}$$

In Equation 4.3, P_{out} is the output laser power and P_{sat} is the laser saturation power given by

$$P_{sat} = \frac{hca_l}{\lambda_l \sigma_a \tau_f}. \tag{4.3}$$

Above, G_{th} is the fractional threshold gain ($G_{th} = (L_c + T_{OC})/2$, with L_c = round-trip cavity loss = 1.7% [Baylam et al., 2018]), a_l is the effective laser beam area, and P_{sat} was determined as 1928 mW. By using the slope of the power-dependent repetition rate data [see Figure 4.2a] together with Equations 4.1 and 4.2, Q_0, was found as 0.016%.

During the SQS operation, the free-running wavelength shifted from 2097 nm to 2091 nm, as shown in Figure 4.2c, with a spectral jitter of about 1 nm, and the spectrum was broadened to almost twice its CW width. We expect that the spectral jitter could be reduced with more precise control of the M1-M2 separation.

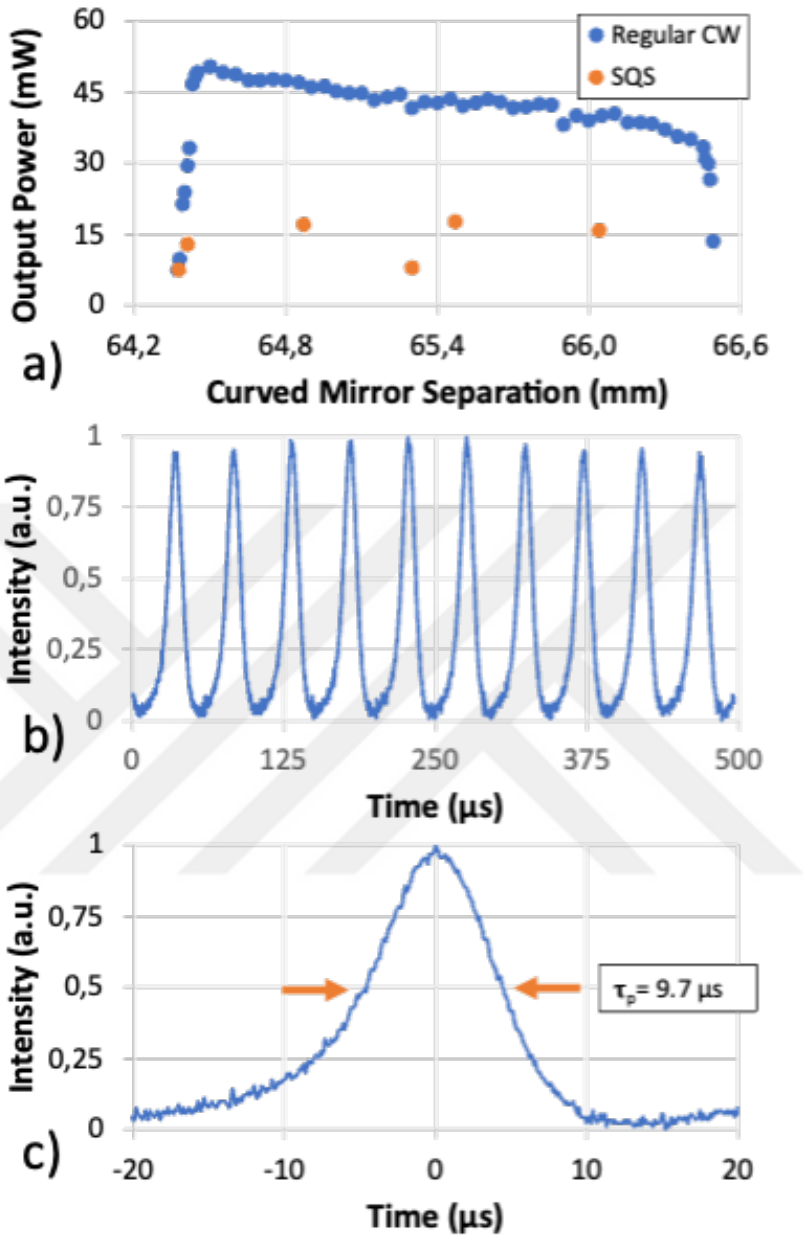

Figure 4.1: (a) Measured variation of the output power for CW and SQS operations as a function of the M1-M2 mirror separation, (b) pulse train recorded over 0.5 ms time window at the mirror separation of 66.04 mm, and (c) measured single pulse profile at the mirror separation of 66.04 mm.

4.2 On the Mechanism Behind SQS

As discussed in the introduction, SQS operation has been observed in other Tm^{3+} doped lasers and various mechanisms have been proposed for the initiation of SQS

[Zu et al., 2020, Zhang et al., 2018, Beyatlı et al., 2020, Zhang et al., 2020a, Kang et al., 2022, Razdobreev and Shestakov, 2006, Cai et al., 2015, Wu et al., 2015]. In particular, the study performed in [Zu et al., 2020] observed a wavelength shift after SQS operation was initiated and an SQS threshold behavior was observed in [Razdobreev and Shestakov, 2006]. Both of these effects were also observed in our SQS experiments. Hence, although further work is required to accurately analyze the detailed nature of the initiation mechanism of SQS, we believe that it is due to an interplay of numerous mechanisms including ESA, GSRA, TDL, dynamic chaos as well as additional concentration dependent effects and other population dependent energy transfer mechanisms.

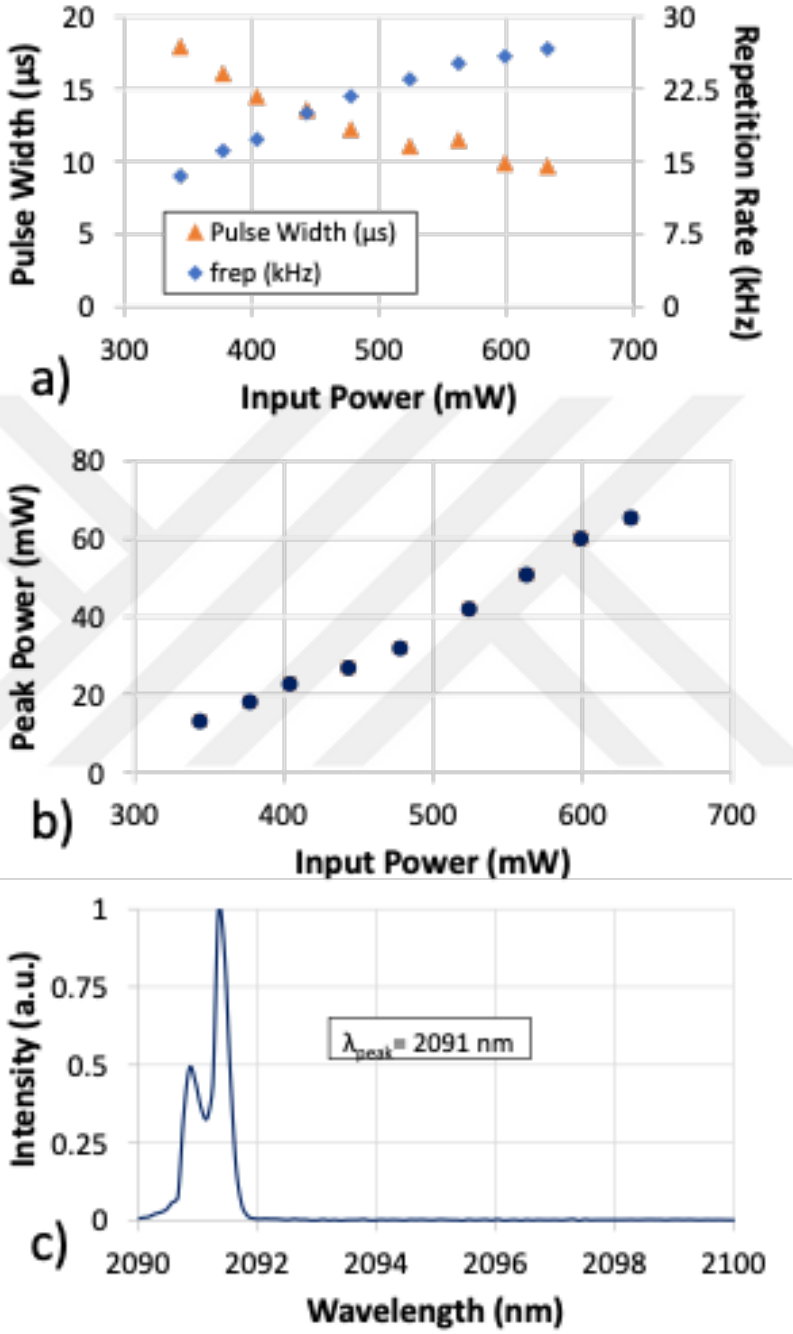

Figure 4.2: (a) Measured variation of the pulse width and repetition rate as a function of the input pump power during SQS operation, (b) measured variation of the peak power as a function of the input pump power, and (c) measured laser output spectrum during SQS operation.

Chapter 5

SYNTHESIS AND CHARACTERIZATION OF PRISTINE AND THULIUM-DOPED ZnS AND ZnSe POWDERS

5.1 Introduction

In the following sections of the thesis, the focus will shift towards obtaining Tm-doped ZnS and ZnSe materials. As discussed earlier, ZnS and ZnSe offer a wider transparency range, extending up to 14 μm and 20 μm, respectively, and possess better thermal conductivity with values of 16.7 and 18 $Wm^{-1}K^{-1}$. These characteristics make thulium-doped ZnS and ZnSe highly attractive candidates for high-power lasers and optical parametric oscillators in the mid-wave infrared (MWIR) region. The research will delve into the synthesis and characterization of Tm-doped ZnS and ZnSe materials, exploring various fabrication techniques and optimizing the doping processes to achieve the desired properties. The goal is to develop efficient and high-performance Tm:ZnS and Tm:ZnSe lasers that can operate effectively in the MWIR spectral range.By investigating these materials, this work aims to contribute to the advancement of laser technology in the MWIR region and explore their potential applications in various fields, including high-power laser systems and MWIR optical parametric oscillators. The successful development of Tm-doped ZnS and ZnSe materials will open up new possibilities for research and applications in the MWIR domain.

High-energy ball milling is a method of mechanochemical synthesis that provides a flexible and effective way to synthesize various materials. In this procedure, the initial materials are subjected to high-energy impacts from milling balls, which cause chemical reactions and structural modifications. One of the key benefits of high-energy ball milling is its simplicity, which necessitates basic equipment and

processes. Compared to other synthesis methods, it is also a more affordable process. High-energy ball milling is also environmentally friendly because it doesn't use solvents and produces less hazardous waste. Rapid reaction kinetics are another benefit of high-energy ball milling. Since solid-state diffusion is encouraged by the strong mechanical forces used in milling, the reaction rates are accelerated relative to conventional synthesis techniques. Additionally, room-temperature high-energy ball milling can be used, negating the necessity for high-temperature processing. Overall, high-energy ball milling is an excellent method for creating new materials since it is straightforward, economical, environmentally friendly, quick to react, and able to carry out reactions at room temperature. Due to these benefits, it is frequently employed in various scientific and commercial applications.

Powder particles are repeatedly deformed, fractured, and welded during high-energy ball milling. This procedure aims to produce uniform, fine-grained materials with improved characteristics. Following is a description of the high-energy ball milling synthesis mechanism. The procedure starts with adding the necessary powder materials to the milling container, commonly a cylindrical vessel constructed of a substance compatible with milling, like stainless steel or tungsten carbide. Milling mediums, such as balls or cylinders, are introduced to the container along with the powder ingredients. These milling media deliver the powerful impact and shear pressures necessary for the mechanical alloying. The medium and powder ratios are generally kept in proportion to enable effective milling. After sealing the milling container, the ball-milling process begins. Rapid rotation of the container around its axis causes the milling media and materials to clash. The impact and shear forces generated by the impacts cause the powder particles to deform, fracture, and weld. Because of the continuous impacts of the milling media, the high-energy ball milling process causes plastic deformation of the powder particles. The particles undergo stretching, fragmentation, and flattening as shown in Figure 5.1

High-energy collisions can cause plastic deformation and cold welding of powder particles. When materials collide at high speeds, the diffusion of the atoms over

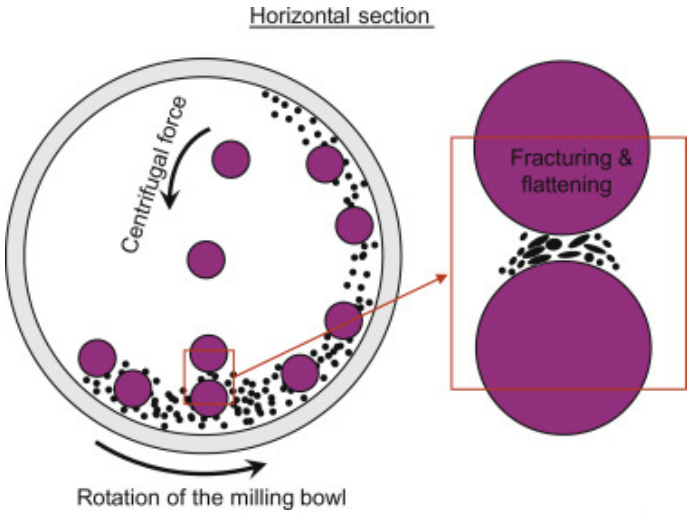

Figure 5.1: Diagram showing how the ball and powder mixture move, adapted from [Faraji et al., 2018]

the contact interface can cause them to bond. The powder particles are constantly fractured and re-welded due to the repetitive impact and deformation cycles. New interfaces occur between the broken surfaces, enabling atoms to diffuse and solid-state alloying to form. The mechanical alloying process is run for a predetermined period to achieve the required degree of mixing and homogeneity of the powder materials. Depending on the system and the required quality, the milling time varies. Once the necessary milling time has been attained, the powder is collected. The powder particles have smaller average grain sizes than the original ingredients and gets smaller with increasing milling time.

The precise synthesis mechanism and results of high-energy ball milling can vary depending on milling speed, ball-to-powder ratio, milling time, milling atmosphere, temperature and powder characteristics such as particle size and composition. The milling speed is typically determined by the milling machine and may not be easily adjustable. On the other hand, the ball-to-powder ratio and milling time can be optimized to achieve desired results. In a previous study by [Oztulum, 2022], the optimization of these parameters for ball milling was performed. As a result, the specific optimization parameters of the ball milling process will not be investigated

in detail in the current thesis, as they have already been determined in the previous research.

Several important powder qualities need to be considered to obtain a transparent material from powder. These qualities can significantly impact the material's final transparency and optical properties. Particle size is a crucial factor in achieving transparency. Smaller particle sizes are desirable as they reduce light scattering and improve transparency. Fine powders with narrow size distributions are preferred to avoid light scattering caused by significant variations in particle size. Particle shape also plays a role in light scattering and transparency. Irregular or non-spherical particles tend to scatter light more than spherical particles. Therefore, powder with more uniform and spherical particle shapes can enhance transparency. The purity of the powder is essential to minimize impurities that can cause light absorption or scattering. Impurities can introduce coloration or create defects that scatter light, reducing transparency. High-purity powders are preferred for transparent materials because crystal structure and particle homogeneity impact transparency. Crystalline materials with a well-ordered structure and uniform composition exhibit better transparency than materials with structural defects or compositional variations.

Surface smoothness is another important factor to consider. Rough or textured surfaces can cause light scattering, leading to reduced transparency. Powders with smooth particle surfaces are preferred to minimize scattering effects. Powder particles with low porosity are preferred for transparent materials. Porosity can scatter and absorb light, diminishing transparency. Powders with dense and compact particle structures are desirable to minimize porosity and enhance transparency. Controlling and optimizing the refractive index of the powder material is crucial. It is essential to match the refractive index of the interface material to the surrounding medium to reduce light reflection and refraction at interfaces. This aids in establishing greater transparency.

5.2 Synthesis and Characterization of Pristine Samples

To prepare samples for the ball milling process, a stoichiometric ratio of high-purity Zn (GoodFellow, 99.9%), S (Sigma Aldrich, 99.998%), and Se (Alfa Aesar, 99.999%) was weighed and placed into stainless steel SPEX vials under Argon atmosphere inside a glove box. Three large and three small stainless stell balls were also added as milling media to aid in the milling process. The vials containing the sample materials and milling media were then placed into a ball milling machine (SpexSamplePrep 8000D) for a total milling time of 2 hours, consisting of 30 minutes of milling followed by a 1-minute rest cycle. This milling procedure was repeated until the total milling time was reached. After the milling process, the vials were opened inside the glove box, and the synthesized powders were transferred to sample holders for further characterization. The resulting powders for both ZnS and ZnSe are shown in Figure 5.2a and Figure 5.3a, respectively. It is worth noting that the colors of the synthesized powders for both materials appeared dark compared to the commercial powders of ZnS (Figure 5.2c) and ZnSe (Figure 5.3c).

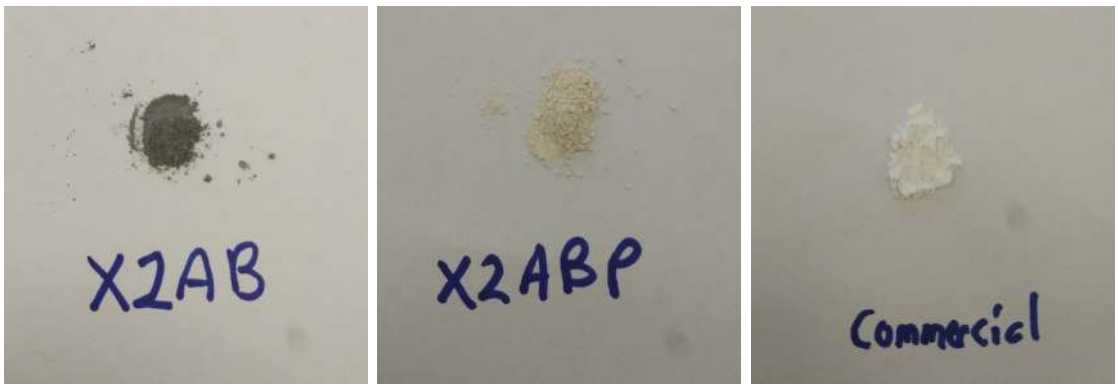

(a) (b) (c)

Figure 5.2: Images of (a) X2AB, unpurified ZnS, (b) X2ABP, purified ZnS, (c) and commercial ZnS powder

To investigate the purity and phase of the synthesized powders, X-ray diffraction (XRD) measurements were performed using a Rigaku Miniflex X-ray diffrac-

(a) (b) (c)

Figure 5.3: Images of (a) X4A, unpurified ZnSe, (b) X4ABP, purified ZnSe, (c) and commercial ZnSe powder

tometer. The XRD measurements were conducted with the following parameters; voltage: 40kV, current: 15 mA, X-ray source: Cu-Kα, wavelength: 1.54 $\mathring{A}$, scanning range: 10° to 90°, scanning speed: 10°/min. These parameters were chosen to obtain diffraction patterns that can provide information about the crystal structure and phase composition of the synthesized powders. By analyzing the XRD patterns, the presence of specific diffraction peaks can be identified, which correspond to the crystal planes of the materials present in the sample. The XRD measurement results for ZnS and ZnSe powders are presented in Figure 5.4 and Figure 5.5, respectively.

The XRD pattern of the ZnS powders (labeled as X2A and X2B) obtained from different SPEX vials but with the same ball-milling conditions shows predominantly the cubic sphalerite phase. However, there are wide bumps observed under the peaks, indicating the presence of additional phases or impurities. Traces of excess Zn and S are also detected in the XRD pattern. For ZnSe, the XRD pattern exhibits slight bumps around the Zn and Se peaks, suggesting the presence of excess elements. Peaks corresponding to the cubic phase are also observed. The highest peak for ZnS is observed at a 2θ angle of 28.5, corresponding to the (111) plane, while for ZnSe, the highest peak is observed at a 2θ angle of 27.2, corresponding to the (111) plane. It is noteworthy that while both the ball-milled and commercial ZnS powders

exhibit the highest peak in the (111) direction, the situation is different for ZnSe powders. The highest peak for the commercial ZnSe powder is observed at a 2θ angle of 45.2, corresponding to the (220) direction. The dark color of the ball-milled powders and the presence of excess element peaks in the XRD patterns suggest the need for further purification. As a result, the powders were subjected to annealing in an inert gas flow at high temperature. The melting points of the elements and compounds are provided in Table 5.1.

Table 5.1: Melting points of materials used

Material	Melting Point (°C)
Zn	419.5
S	115.2
Se	221
ZnS	1850
ZnSe	1525

The purification process was carried out using a vertical furnace, as shown in Figure 5.7, under a continuous flow of argon gas. The synthesized powders were carefully inserted into quartz tube within the glove box, and the system was sealed. Subsequently, the tube was placed in the furnace, and the furnace was heated to the desired temperature under a continuous argon flow. After the purification process, the XRD peaks exhibited higher amplitudes and lower full width at half maximum (FWHM), indicating an increase in particle size and the elimination of excess peaks. For ZnSe, the purification conditions were optimized according to the work of Oztulum et. al. , and the powders were subjected to a purification temperature of 750 °C for two days under argon flow [Oztulum, 2022]. The purification resulted in improved XRD patterns, with higher peak amplitudes and narrower peaks, indicating increased particle size and reduced impurities.

Regarding ZnS, different purification temperatures were tested, and the best re-

sults were obtained by purifying the powders at 750 °C for two days under argon flow. After purification, the XRD patterns showed the presence of Wurtzite 8H and Wurtzite 10H peaks, indicating the formation of the high-temperature phase of ZnS. In bulk materials, the cubic phase of ZnS transforms to the Wurtzite phase at temperatures around 1020 °C. However, due to the small particle size and high surface energy of the powders, some particles underwent the transformation to the hexagonal phase at lower temperatures. The presence of the hexagonal phase is undesirable as it exhibits different refractive index and density compared to the cubic phase. This difference in refractive index at grain boundaries can lead to reflections and reduced transparency, as well as birefringence.

To gain an understanding of the desired purity and phase, commercial ZnS (Sigma Aldrich, 99.99%) and ZnSe (Sigma Aldrich, 99.99%) powders were also measured using XRD. The XRD patterns of the commercial powders were fairly similar to those of the purified powders. In the case of commercial ZnS powder, the presence of the Wurtzite phase was also observed.

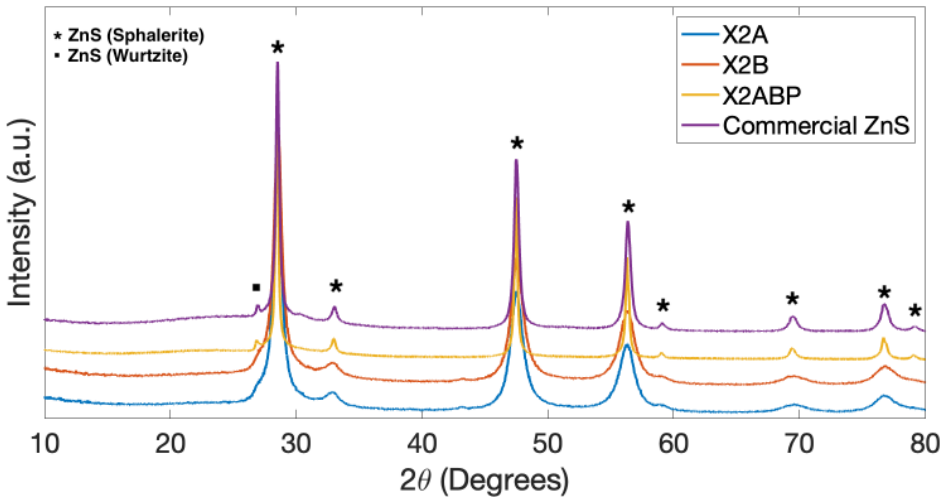

Figure 5.4: XRD measurement of X2A, X2B, X2ABP coded and commercial ZnS powders

Additionally, the effect of sieving was investigated using sieves with different

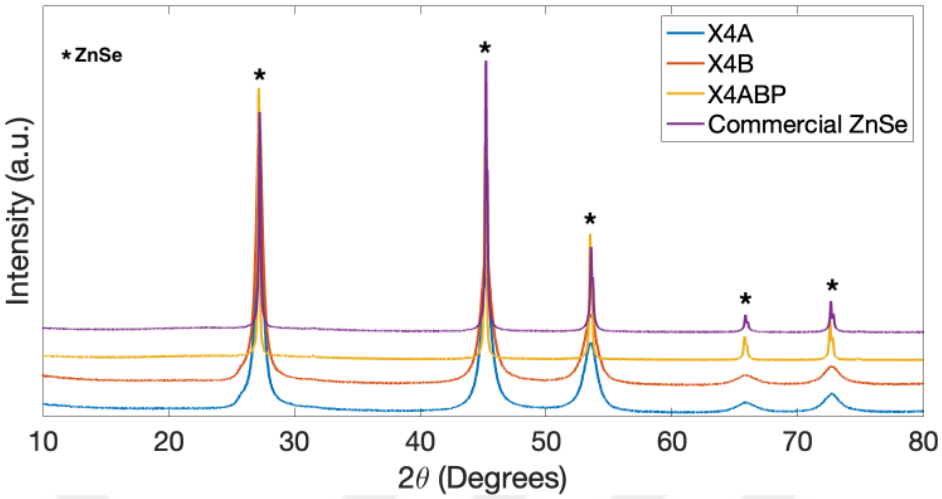

Figure 5.5: XRD measurement of X4A, X4B, X4ABP coded and commercial ZnSe powders

mesh sizes. However, it was observed that the sieves used were not as sensitive as desired. Therefore, the sieved powders were divided into two categories based on the sieve with a finer mesh. The purified powders were then coded as X11ABP, X11ABP2, and X11ABP3. The purification processes were conducted at temperatures of 500 °C, 750 °C, and 850 °C, respectively, for durations of 4 days, 2 days, and 2 days, respectively. However, no significant effect of sieving was observed. It was found that the X11ABP3GT106 samples showed higher peaks and narrower full width at half maximum (FWHM) compared to the X11ABP3LT106 samples as expected.

The average crystallite size of the synthesized powders can be calculated using the Scherrer Equation 5.1:

$$D = \frac{K\lambda}{\Gamma cos(\theta)} \tag{5.1}$$

where D is the average particle size, K is the shape factor (typically taken as 0.9), λ is the X-ray wavelength, Γ is the full-width at half-maximum (FWHM) of the peak, and θ is the Bragg angle. Using the values $\lambda = 0.154$ nm, $\Gamma = (0.0044, 0.0062, 0.0030, 0.0030)$, and $2\theta = (28.48, 28.5, 27.16, 27.23)$, D is calculated

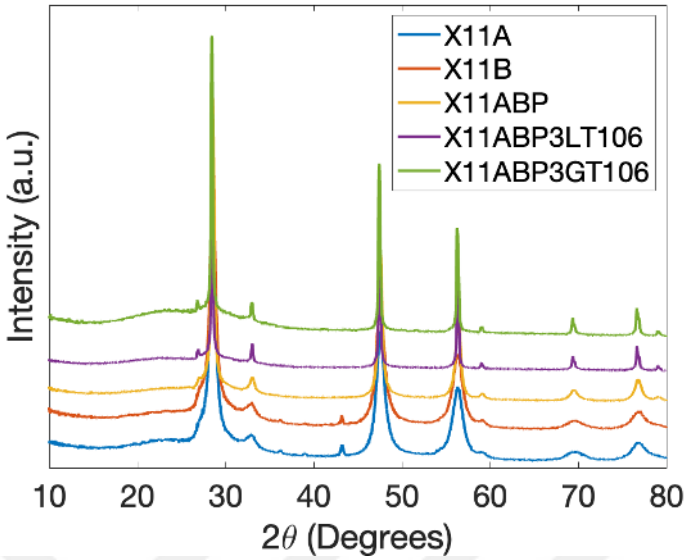

Figure 5.6: XRD measurement of X11A, X11B, X11ABP coded ZnS powders

as 31 nm for ball-milled ZnS, 23 nm for commercial ZnS, 48 nm for ball-milled ZnSe and 48 nm for the commercial ZnSe.

To characterize the morphology of the powders Zeiss Ultra Plus Field Emission Scanning Electron Microscope is used. SEM images were taken before and after the purification. For both ball-milled ZnS and ZnSe powders, textural changes after the purification was quite similar. Firstly, the surface roughness was decreased with purification. The shape of the particles were smoother however shapes were non-spherical and irregular. Also, for three different magnification, the overall particle size increased. However, for both particles, particle size distribution was quite high and didn't improve greatly with purification. There were particles as big as 10 μm. There were agglomerated particles. Agglomeration is unwanted since it may include internal defects and voids which behave as scattering centers. Commercial ZnS powder which is grown by chemical vapor deposition showed very large homogeinity in particle size distribution and has spherical particles as shown in Figure 5.10. All particles were about 2 μm in size. For the commercial ZnSe powder (see Figure 5.13), particle size and morphology were quite similar to the ball-milled powder.

Figure 5.7: Purification setup

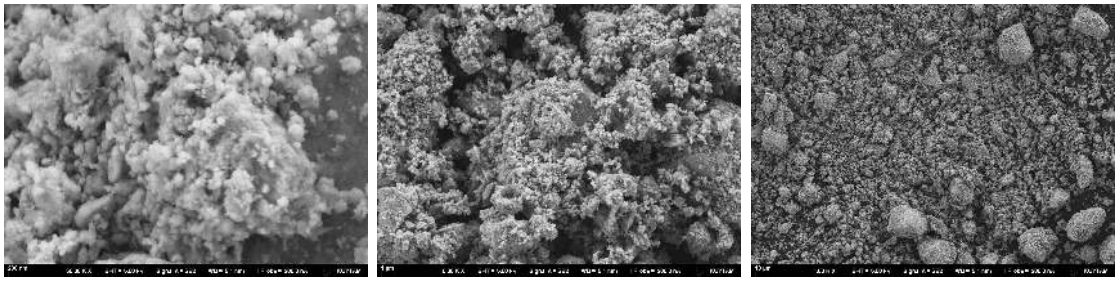

(a) (b) (c)

Figure 5.8: SEM images of X2 coded ZnS powder with (a) 200 nm, (b) 1 μm (c) 100 μm scale bars

5.3 Thulium doping

To synthesize thulium-doped powders, high-energy ball-milling was employed. Stoichiometric amounts of Tm (Nanografi, 99.5%), Zn (GoodFellow 99.9%), and Se

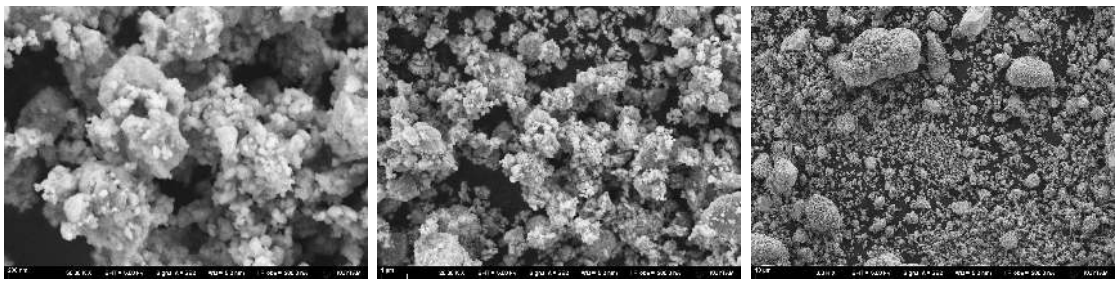

(a) (b) (c)

Figure 5.9: SEM images of X2ABP coded purified ZnS powder with (a) 200 nm, (b) 1 μm (c) 100 μm scale bars

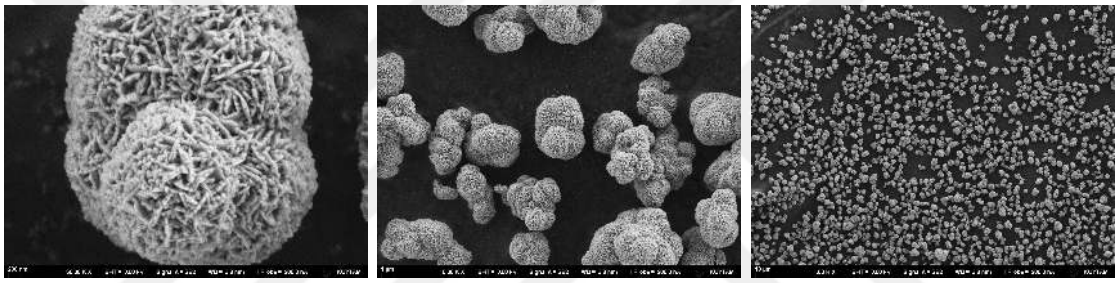

(a) (b) (c)

Figure 5.10: SEM images of commercials ZnS powder with (a) 200 nm, (b) 1 μm (c) 100 μm scale bars

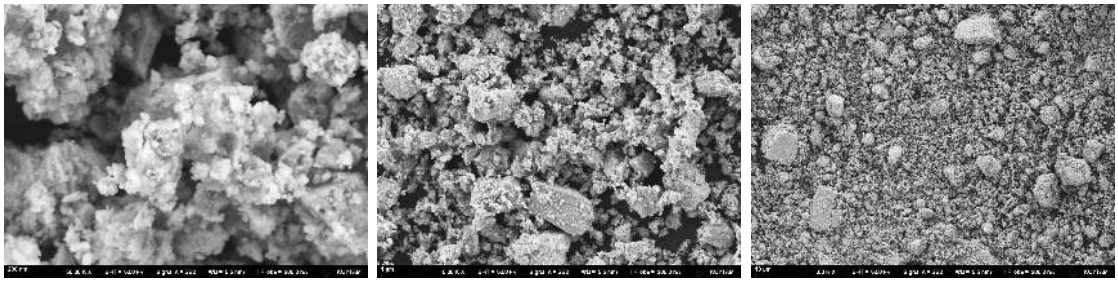

(a) (b) (c)

Figure 5.11: SEM images of X4 coded ZnSe powder with (a) 200 nm, (b) 1 μm (c) 100 μm scale bars

(Alfa Aesar 99.99%) were used for the synthesis of Tm:ZnSe. The same optimized conditions were applied during the ball-milling process.

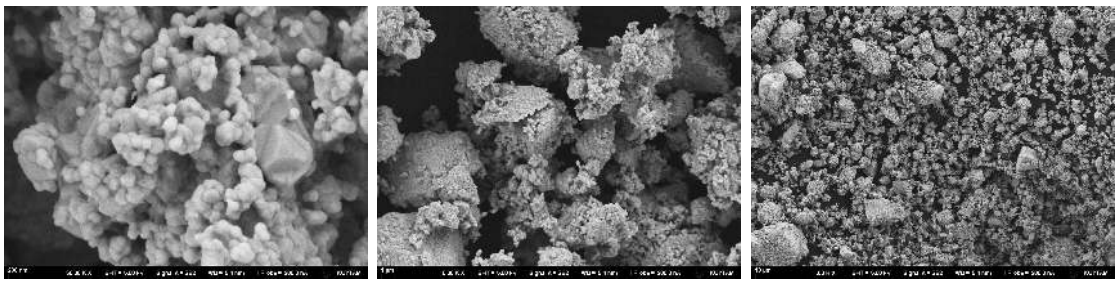

(a) (b) (c)

Figure 5.12: SEM images of X4ABP coded purified ZnSe powder with (a) 200 nm, (b) 1 μm (c) 100 μm scale bars

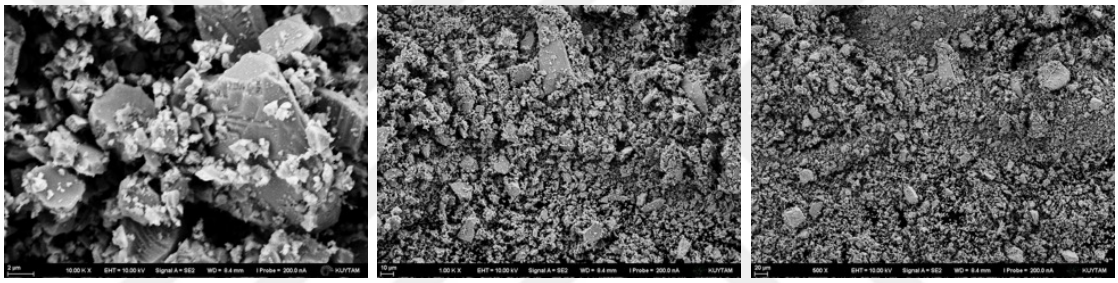

(a) (b) (c)

Figure 5.13: SEM images of commercials ZnSe powder with (a) 2 μm, (b) 10 μm (c) 20 μm scale bars

To assess the success of doping, various properties such as bandgap, lattice parameter, and photoluminescence spectrum of the synthesized powders were investigated. However, it is important to note that stoichiometric ratios can vary depending on the pre-synthesis and synthesis conditions. In order to determine the actual amounts of thulium in the samples, Inductively Coupled Plasma Mass Spectrometry (ICP-MS) measurements were conducted using an Agilent 7700x instrument. The results of the ICP-MS measurements are presented in Table 5.2. It was observed that the desired stoichiometries deviated slightly from the desired ratios after synthesis. After Purification ICP-MS measurements were repeated and a change in the stoichometry was observed as shown in Table 5.3.

Table 5.2: Thulium amount in the samples as measured by ICP-MS before purification

Sample Name	Desired Tm Amount (at. %)	Detected Tm amount (at. %)
X13A	3	2.70
X13B	0	0
X14A	1	1.06
X14B	5	4.92
X15A	0.5	0.43
X15B	1	1.07
X16A	0.25	0.39
X16B	0.75	0.72

Table 5.3: Thulium amount in the samples as measured by ICP-MS after purification

Sample Name	Detected Tm amount (at. %)
X13AP	3.51
X13BP	0
X14AP	1.16
X14BP	5.63

After determining the amounts of thulium in the powders, their reflectance was measured using a SHIMADZU UV-3600 UV-VIS-NIR Spectrophotometer. The reflectance data was then utilized in the Kubelka-Munk equation (Equation 5.2) to determine the band gap of the powders.

$$\Lambda h\nu = \beta(h\nu - E_g)^n \tag{5.2}$$

In Equation 5.2, the symbol ν represents the frequency, β is an arbitrary constant, E_g denotes the band gap energy, and n is a constant. For indirect band gap materials, n takes a value of 1/2, while for direct band gap materials, n is equal to 2. The value of Λ in Equation 5.3 is determined accordingly.

$$\Lambda = \frac{(1-R)^2}{2R} \tag{5.3}$$

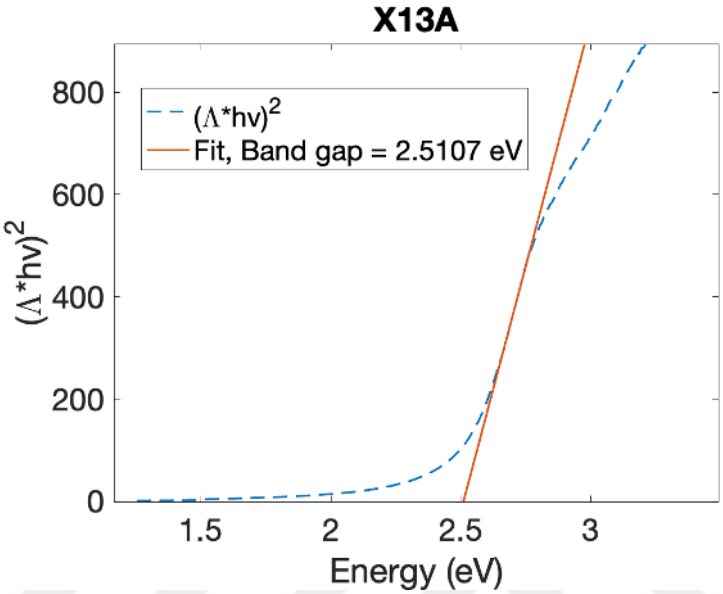

Figure 5.14: Kubelka-Munk equation fitted to the X13A data

The calculated band gaps as a function of the Tm amount are presented in Figure 5.15. It is crucial to keep in mind that doping a semiconductor with a rare earth ion like Tm might not have a direct and noticeable impact on the semiconductor's band gap. The configuration and energy levels of a semiconductor's valence and conduction bands, as well as other aspects of its intrinsic electronic structure, are what essentially influence a semiconductor's band gap. Doping inserts impurities into the semiconductor lattice, which may indirectly affect the electronic characteristics of the material. The direct effect on the band gap is often not very significant. As ZnSe has a band gap of about 2.7 eV, we saw a shift in the band gap as a function of Tm doping and a very broad dispersion in the band gaps in our investigation. This can be attributable to the ball-milled powders having too much of the original components. The powders underwent additional purifying procedures to overcome this problem. One specific data point in the graph represents a Tm doping level of 0.75% and displayed a much darker color than the other powders. It is necessary to address and resolve the surplus elements that are indicated by this darker color

through purification processes.

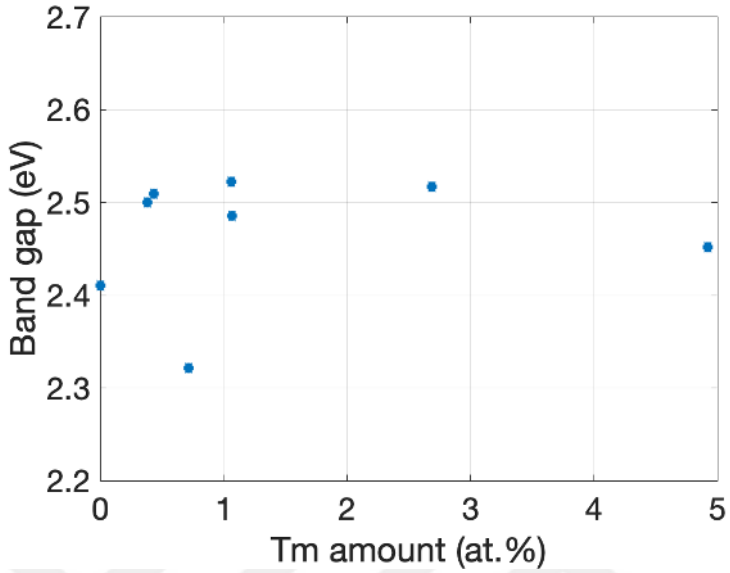

Figure 5.15: Band gap (eV) as a function of Tm amount before purification

After purification the dispersion in the band gaps of the synthesized powders was reduced significantly as shown in Figure 5.16. Up to the 3 at. % of doping levels, the band gap was fairly constant around 2.66 eV and reduced when doping is increased.

Lattice parameter refinement is a method for precisely calculating the lattice parameters of crystalline materials. Lattice parameters describe the size and form of a crystal lattice's unit cell. A crystal lattice is a recurrent, three-dimensional arrangement of atoms used in crystallography. The unit cell is the smallest repeating unit of the lattice and has dimensions determined by the lattice parameters. The lengths and angles between the cell's edges define the characteristics of the unit cell. Using experimental methods and data analysis, lattice parameters are refined to get closer to their exact values. Data collection for this process uses methods like X-ray diffraction. The gathered diffraction patterns offer details on the beam angles and intensities, which can be utilized to deduce information on the crystal lattice. The Miller indices of the diffracted peaks are then calculated using indexing and data

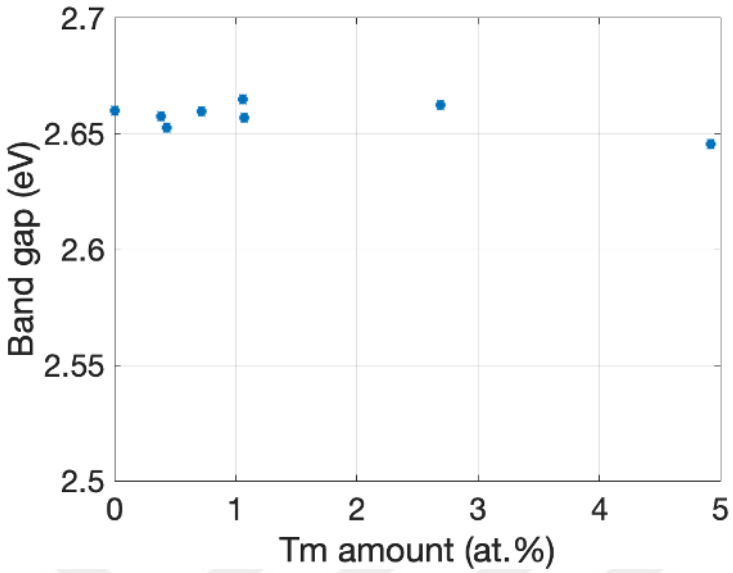

Figure 5.16: Band gap (eV) as a function of Tm amount after purification

reduction techniques using the collected data. These indices are connected to the crystal lattice's crystallographic planes. The data is further processed by eliminating background noise, accounting for instrument effects, and isolating proper peak positions and intensities. The revised lattice parameters are determined by comparing the retrieved peak positions to theoretical values based on various assumed lattice parameters. The disparities between the calculated and actual peak positions are reduced by using mathematical models and optimization procedures. The best-fit lattice parameter values are eventually reached through this iterative approach.

Accompanying the refined lattice parameters are estimates of their uncertainties. Statistical analysis techniques are used to quantify the precision and reliability of the refined values, taking into account factors such as measurement errors and systematic effects. Lattice parameter refinement is crucial for understanding the structural properties of materials as the lattice parameters influence various physical properties such as mechanical behavior, electrical conductivity, and thermal expansion. Accurate determination of lattice parameters enables to study crystal structures, phase transformations, and relationships between structure and properties in materials.

In the process of Tm doping in ZnSe, thulium atoms are substituted for zinc atoms. The ionic radius of Zn^{2+} is 88 pm, while that of Tm^{3+} is 102 pm. Doping is expected to cause a change in the lattice parameter. To determine the lattice parameter, LaB_6 is used as a reference material. XRD measurements are carried out using a 4 to 1 ratio of powders for ZnSe and LaB_6, respectively. The obtained peaks are refined to calculate the lattice parameters. The relationship between lattice parameter and atomic percentage of thulium content is depicted in Figure 5.17. All the doped powders exhibited higher lattice parameters compared to the undoped powder. However, after the purification lattice constants were fairly close to each and to the theoretical value, as shown in Figure 5.18. The lattice parameters for cubic ZnSe and ZnS are 5.66 $\mathring{A}$ and 5.39 $\mathring{A}$, respectively.

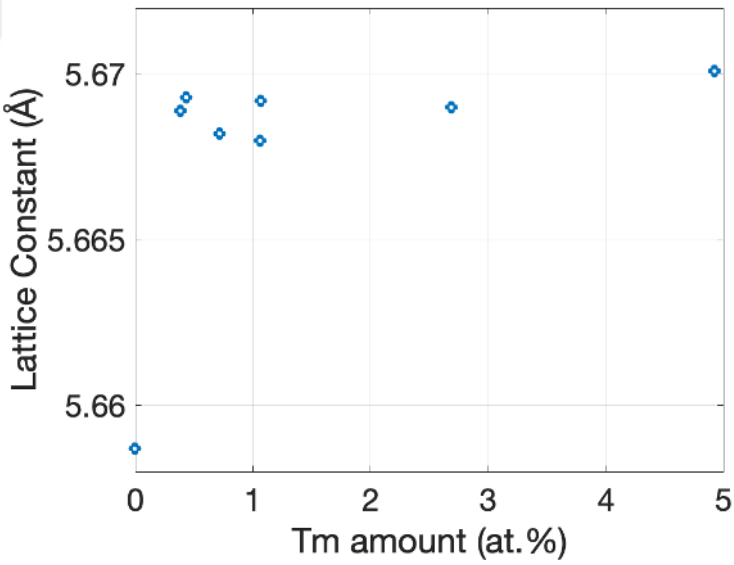

Figure 5.17: Lattice parameter as a function of Tm amount before purification

The most reliable method to confirm the success of doping is through absorption measurements. However, this requires the availability of synthesized transparent materials. To overcome this challenge, the photoluminescence (PL) spectrum can be employed. Doped Tm ions function as luminescent centers, allowing for the use of

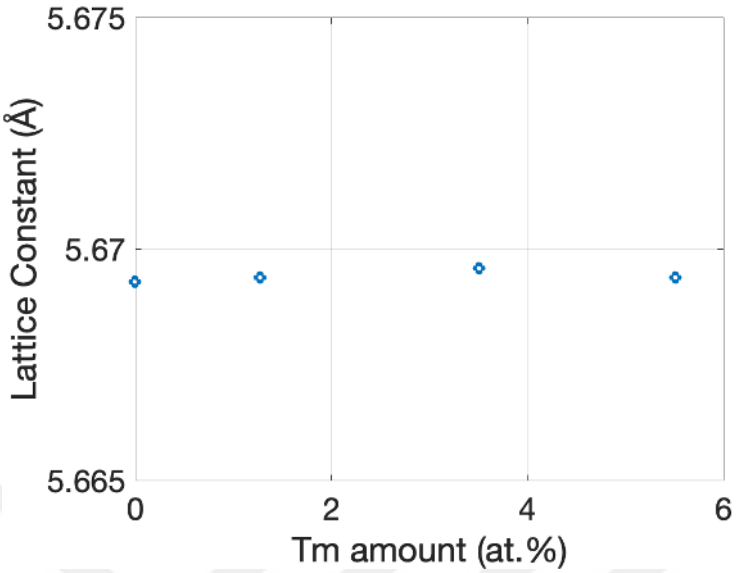

Figure 5.18: Lattice parameter as a function of Tm amount after purification

PL spectrum as an alternative. Before conducting the PL spectrum measurement, the powders were cold-pressed in 10 mm dies at a force of 10g Tons. Subsequently, PL spectra were collected within the wavelength range of 1600 nm to 2000 nm, using three different excitations: 680 nm, 700 nm, and 800 nm. However, for both the undoped and doped powders, no emission was observed under any of the excitation wavelengths.

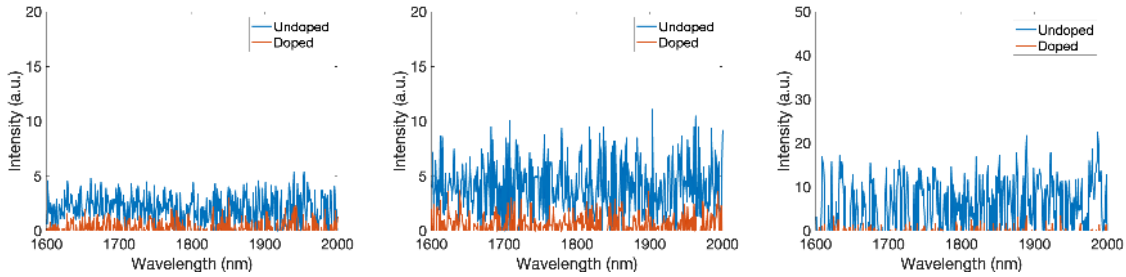

(a) (b) (c)

Figure 5.19: Photoluminescence spectrum of cold-pressed Tm:ZnSe undoped and 5% doped pelets under (a) 680 nm, (b) 700 nm (c) 800 nm excitations

Chapter 6

SINGLE AND POLYCRYSTAL GROWTH OF ZnS AND ZnSe

6.1 Introduction

Powder characteristics alone are not sufficient to produce a transparent material. By removing porosity, improving particle packing, and fostering densification, powder processing procedures like compaction, sintering, or melting also play a significant role in obtaining transparency. To make a transparent material from powder, it is therefore necessary to combine adequate powder properties with appropriate processing methods.

Chemical vapor transfer (CVT) uses a gaseous phase to transport and deposit chemicals. It involves the controlled reactivity of volatile compounds that act as transport agents for moving the desired substance from a source to a deposition base. CVT is commonly employed in thin film deposition, crystal growth, and material synthesis. The transport agent should have a high vapor pressure at the reaction temperature. It is put close to the source material. The reaction vessel or reactor regulates the temperature and pressure parameters. The process starts with the reaction between the source material and the transport agent at an elevated temperature. This reaction forms volatile compounds or complexes that vaporize and become gaseous species. The gaseous transport species carry the desired material from the source to the deposition substrate, facilitated by the transport agent acting as a carrier gas. The pressure difference between the source and deposition regions drives the transport. The gaseous transport species go through a reversal reaction once they get to the cooler deposition target. A thin film or crystalline structure is created on the substrate by depositing the necessary material there. To obtain the

required deposition characteristics, including growth rate, shape, and composition, variables like temperature, pressure, and reactant concentrations are meticulously controlled and tuned.

Advantages of chemical vapor transfer include the ability to create big single crystals, thin films, and nanostructures with controlled composition and great purity. Additionally, it permits the transfer of substances with chemical reactivity or melting points that differ significantly. The specifics of the CVT process might vary depending on the materials and application, with variable combinations of source materials, transport agents, and reactor conditions employed to obtain the appropriate transport and deposition properties.

Spark plasma sintering (SPS) is a technique that compacts and consolidates powders into solid materials with improved properties. Both electric current and pressure are applied to the powder sample. The process is carried out in an SPS machine equipped with punches, a graphite die, and an electrical power source. The powder material is loaded into a graphite die to begin the procedure. Punches that act as electrodes for the electricity are placed on both ends of the die. The SPS machine heats the die assembly to the required sintering temperature. Different heating techniques, such as resistive, inductive, or microwave, can generate heat. The applied pressure can vary depending on the application. Simultaneously, a pulsed electric current is passed through the punches, flowing through the powder sample. The pulsed current creates localized heating at the contact points between the powder particles. As the pulsed current passes through the powder, sparks or plasma discharges are formed at the particle-particle interfaces due to the high current density. These sparks generate heat through resistive heating, raising the temperature at the contact points. The localized heating promotes enhanced densification and sintering of the powder.

SPS offers quick heating and cooling rates made possible by pulsed current as one of its benefits. In addition to preserving the final material's characteristics, this

can reduce grain growth. The powder is consolidated into a solid by the combined action of pressure, localized heating, and enhanced sintering. The finished product has better density, homogeneity, and mechanical qualities than conventional sintering techniques.

In the literature several studies showed fabrication of transparent ceramics with the Spark Plasma Sintering method. A notable study by Sakjio et al. demonstrated the exceptional transparency of polyscrystalline materials synthesized through SPS [Sakajio et al., 2022]. They showed that the addition of LiF as a sintering aid not only reduced carbon contamination but also facilitated densification by promoting the formation of a liquid phase. Similar results regarding increased transparency have been observed by Frage et al. for Nd:YAG ceramics [Frage et al., 2012]. They found that the addition of certain sintering aids led to improved transparency in the resulting material. Additionally, Furuse et al. successfully demonstrated laser oscillation in Yb^{3+}:Y_2O_3 ceramics fabricated using SPS [Furuse et al., 2018]. This highlights the potential of SPS in producing transparent laser gain media. Furthermore, Lee et al. investigated the fabrication of transparent Yb^{3+}:Y_2O_3 ceramics using a two-step temperature and pressure profile [Lee et al., 2021]. They demonstrated the effectiveness of this approach in enhancing the inline transmittance of the material. These studies collectively showcase the capabilities of the SPS method in synthesizing highly transparent ceramics and its potential for various applications in the field of optics and laser technology.

The Bridgman method, also known as the Bridgman-Stockbarger technique, is widely used for growing single crystals from a melt. It involves controlled solidification of a material to obtain a single crystal with desired properties. The process utilizes a specially designed apparatus called a Bridgman furnace, which consists of a vertical tube or ampoule capable of withstanding high temperatures. To begin the process, the material to be grown as a single crystal is prepared by melting the starting materials. It is essential to carefully control the melt's composition and purity to ensure the crystal's desired properties.

The Bridgman furnace is heated, creating a controlled thermal gradient along the length of the ampoule. Typically, one end of the ampoule is heated while the other end is maintained at a lower temperature. This temperature gradient sets the stage for controlled solidification. As the temperature gradient is established, the melt begins to solidify from the end of the ampoule where the temperature is higher. The solidification front moves downwards along the ampoule as the furnace is either slowly translated or the ampoule is pulled out of the furnace. The movement of the solidification front determines the crystal's growth direction. By carefully controlling the rate of ampoule translation or withdrawal speed, it is possible to control the crystal's growth direction and achieve the desired crystal orientation. This allows to grow crystals with specific orientations. Also, the use of a seed can be employed to promote growth in a specific crystallographic orientation.

During solidification, a single crystal starts to grow from the melt. The crystal is pulled along with the movement of the solidification front, forming a larger, single-crystal structure. Once the crystal growth is complete, the ampoule is cooled to room temperature. In some cases, an annealing process may be performed to relieve any internal stresses or defects within the crystal structure. The Bridgman method enables the growth of large, high-quality single crystals with controlled orientations and compositions. This technique finds applications in various fields, including materials science, semiconductor industry, and solid-state physics.

6.2 Synthesis and Characterization of Chemical Vapor Transport

In the first step, the temperature profile of the two-zone furnace was measured using a thermocouple, with the first heater set to 1080 °C and the second heater set to 1030 °C. Subsequently, the temperature was recorded as a function of the distance from one end of the furnace, as depicted in Figure 6.1.

To synthesize a single crystal of ZnS, a quartz tube with a length of 15 cm

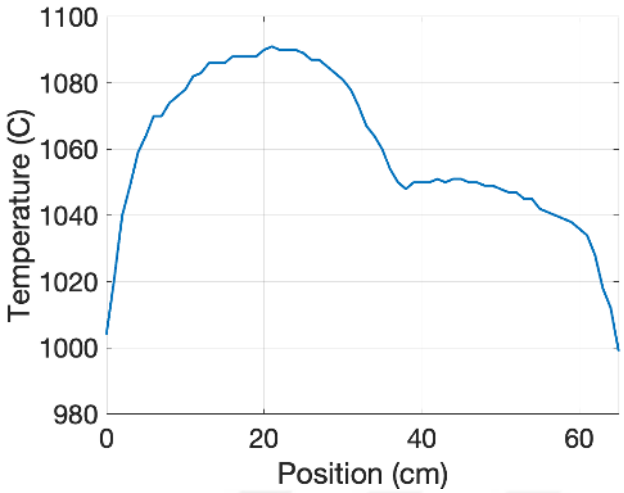

Figure 6.1: The temperature profile of the two zone furnace recorded at 1080 °C and 1000 °C for the first and second heater, respectively.

was utilized. Inside the tube, 1 gram of ball-milled powder, X2ABP, was combined with a transfer agent of 10 mg I_2. Subsequently, the quartz tube was evacuated to a pressure of 10^{-2} Torr using a Schlenk line and sealed. Three quartz tubes, prepared under identical conditions, were positioned at different locations. The first heater around the source area was set to 855 °C, while the second heater around the deposition area was set to 800 °C. Due to their varying positions, all three tubes were exposed to different thermal gradients. Further information regarding the temperatures and positions of the quartz tubes can be found in Table 6.1.

Table 6.1: Positions and the temperatures of samples inside CVT furnace

Sample Name	Tip Position	Tip Temperature	End Temperature
X6A	21	862	805
X6B	27	855	800
X6C	26	855	805

After a period of two weeks, the growth process was completed, and the synthesized materials were subjected to characterization. The images of the synthesized materials, namely X6A, X6B and X6C can be observed in Figure 6.2.

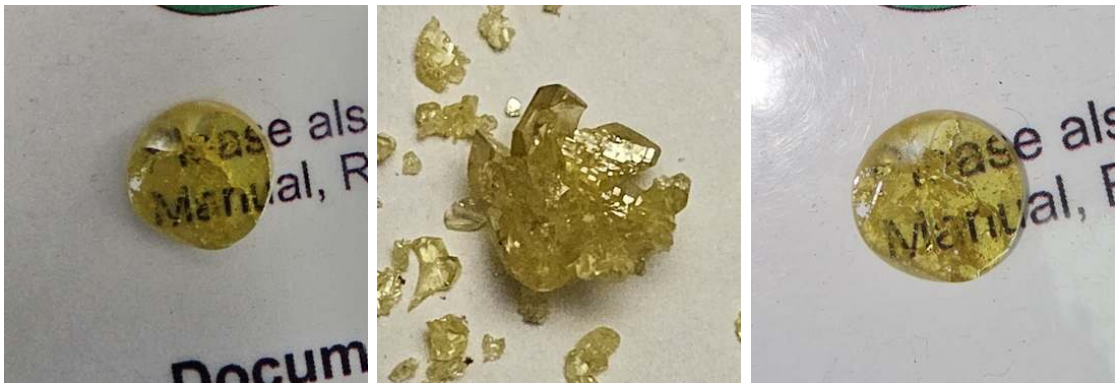

(a) (b) (c)

Figure 6.2: Images of the CVT grown samples (a) X6A, (b) X6B, (c) X6C

It was observed that although the leftmost points of the tubes were maintained at the same temperature of 855 °C, a difference of 5 °C in the deposition target temperature resulted in a significant variation in crystal size. In comparison to X6C, X6A exhibited a higher source temperature. Taking into account the constant temperature zones illustrated in the heat profile (refer to Figure 6.1), it can be inferred that a steeper profile with a higher gradient from the source to the deposition points facilitated the growth of larger crystals.

The synthesized X6C sample exhibited the best transparency in the visible region among all samples. To further investigate its transparency, an FTIR measurement was performed, and the results are illustrated in Figure 6.4. Assuming there are no absorption and scattering losses within the medium, the maximum achievable transmission can be determined using the Fresnel transmission equation, Equation 6.1, at normal incidence. In Equation 6.1, n_1 and n_2 represent the refractive indices of the two media. For ZnS and ZnSe at a wavelength of approximately 10 μm, the refractive indices are 2.199 and 2.393, respectively. As a result, the maximum transmissions for ZnS and ZnSe are calculated to be 74% and 69%, respectively. The X6C sample exhibited a fairly constant transmission of about 40% in the 5-12 μm region. The drop in transmission around 2 μm could potentially be caused by

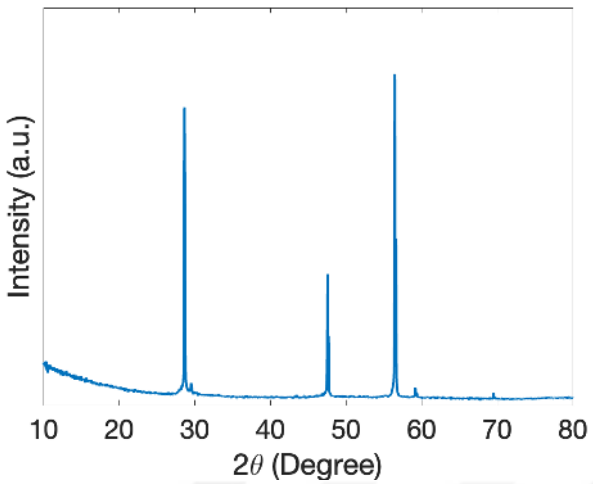

Figure 6.3: XRD pattern of the X6C sample

the presence of voids or grains with nearly the same size, which may lead to Mie scattering effects.

$$\text{Maximum Transmission} = \left(\frac{4n_1n_2}{(n_1+n_2)^2}\right) \times 100\% \tag{6.1}$$

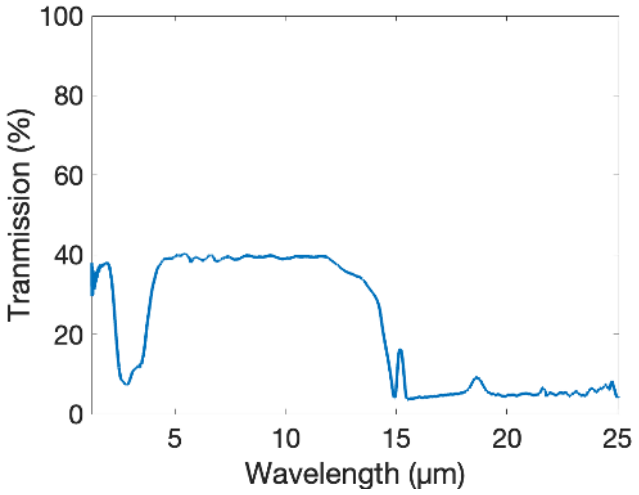

Figure 6.4: Transmission (%) of X6C sample

In contrast, a commercially available polycrystalline ZnSe sample grown via chemical vapor deposition (CVD) demonstrated a transmission curve, as presented

in Figure 6.5. The transmission remained relatively constant at around 70% up to a wavelength of 14 μm.

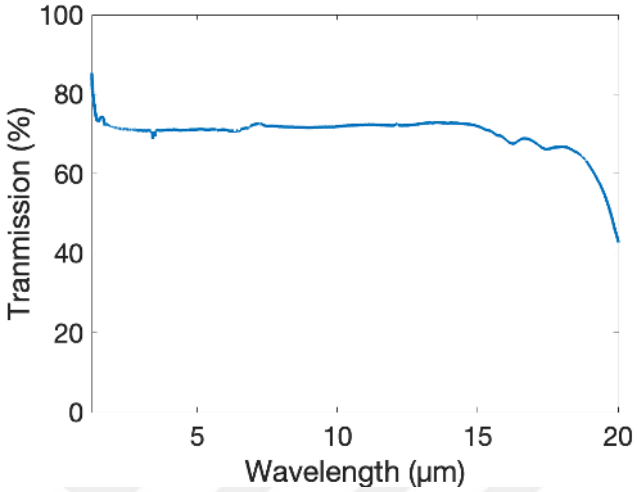

Figure 6.5: Tranmission (%) of commercial ZnSe sample

6.3 Synthesis and Characterization of Spark Plasma Sintering

In the SPS process, graphite dies, punches, and spacers are utilized. Initially, a graphite spacer is positioned within the die. Subsequently, three graphite spacers with the same thickness are placed between the powder and each punch. These steps are carried out inside a glove box under an Argon atmosphere to maintain a controlled environment. Finally, the die assembly, with graphite spacers positioned above and below the punches, is placed inside the SPS machine.

In the synthesis process using SPS, various heat rates, temperature profiles, and pressure profiles have been employed. As demonstrated in the literature [Lee et al., 2021], different temperature profiles, such as two-step profiles, have been shown to accelerate densification, reduce grain growth, and minimize the formation of pores. It is also important to keep the sintering times relatively short to avoid potential carbon contamination from the die, punch, and spacers used in the experiments. For the SPS trials, ball-milled ZnS powder (X7ABP) was used for trials 1-8, while

commercial powder was used for the remaining trials.

In the initial SPS trials, a single-step pressure and single-step temperature profile were employed, with a sintering temperature (T_s) of 850 °C, resulting in a relative density (RD) of 95.3% (Figure 6.6a). Subsequently, a peak temperature followed by sintering at a lower temperature strategy was pursued for the third, fourth, and fifth SPS runs. However, this temperature profile yielded poor results, as indicated by the X7ABPSPS3 and X7ABPSPS4 lines in Figure 6.6. Increasing the peak temperature to 900 °C while maintaining the same sintering temperature of 650 °C yielded nearly the same RD of approximately 95% but with a shorter sintering time. Further increasing T_s to 850 °C produced similar RD to that of SPS2 but with a shorter duration. Applying a similar temperature profile but with a two-step pressure profile resulted in an RD of 92%.

To reduce uncertainties associated with the ball-milled powder, commercial powder was utilized to optimize the sintering profiles. In subsequent experiments, both sintering time and heating rate were adjusted as shown in Figure 6.7bb. Although the sintering time was significantly longer for CPSPS11, slow heating resulted in a decrease in RD from 96.4% to 95.4%. A constant pressure profile and two different temperature profiles were then applied (Figure 6.8a), but there were no significant improvements in RD. Finally, a two-step pressure and temperature profile (Figure 6.8b) with $T_s = 950$ °C yielded an RD of 100%. However, an increase in the Wurtzite phase was observed, as shown in Figure 6.9.

The fabricated pellets exhibited a white color and were not transparent in the visible region. As depicted in Figure 6.11, the increase in relative density (RD) from 95% to 100% resulted in a corresponding increase in transmission in the 10 μm - 15 μm region by 10%. Despite the improvement in transmission in the mid-infrared region, the pellets remained opaque in the visible spectrum.

The use of LiF as a sintering aid was also investigated in the study. LiF has a

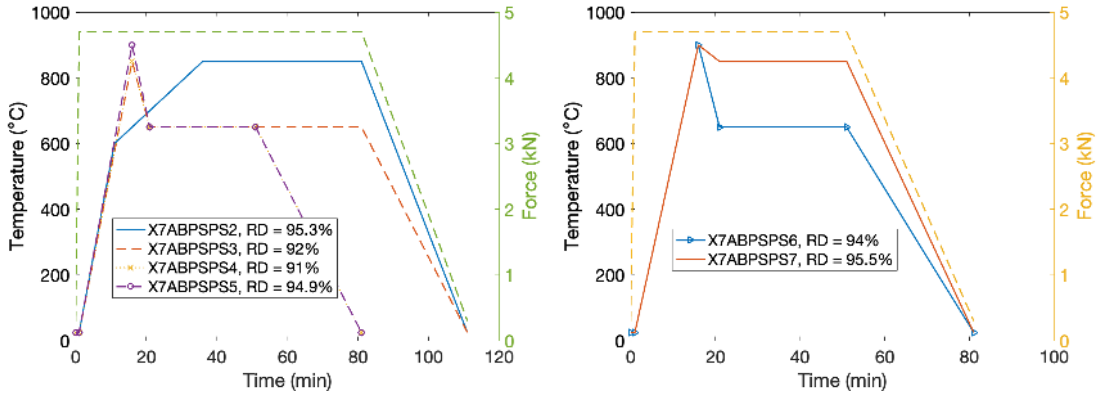

(a) (b)

Figure 6.6: Temperature and pressure profiles for the SPS trials 1 to 7

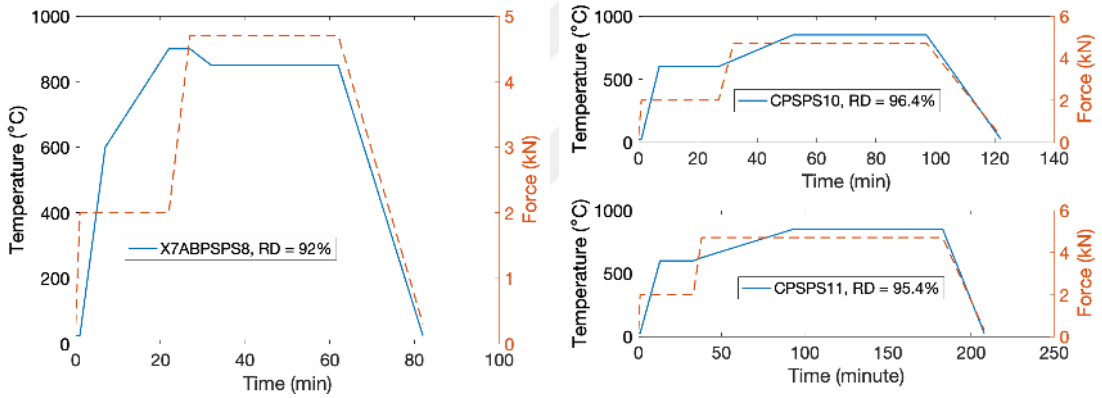

(a) (b)

Figure 6.7: Temperature and pressure profiles for the SPS trials 8 to 11

melting point around 800 °C. The starting amount of LiF was determined based on previous research [Sakajio et al., 2022]. Initially, 0.5 weight % of LiF was mixed with commercial ZnS powder using a mortar inside a glove box. After the SPS process, a decrease in relative density (RD) was observed, from 95.5% to 93.8%. The FTIR results (Figure 6.12) also showed a decrease in transmission.

To further explore the effect of LiF, commercial ZnS powder was ball-milled with 0.5 weight % of LiF for 30 minutes. The resulting ball-milled powder was then sub-

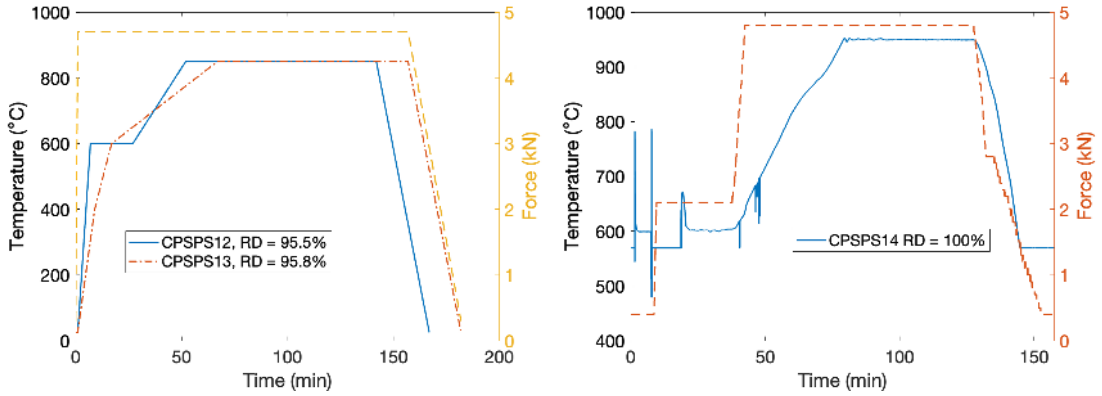

(a) (b)

Figure 6.8: Temperature and pressure profiles for the SPS trials 12 to 14

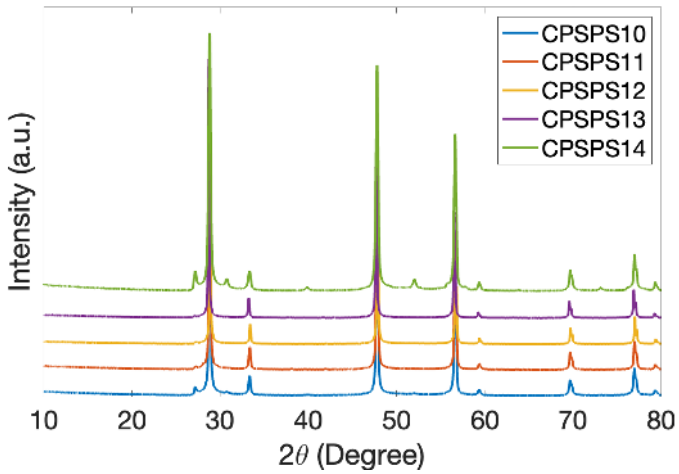

Figure 6.9: XRD measurement of CPSPS10, CPSPS11, CPSPS12, CPSPS13, CPSPS14 coded ZnS powders

jected to SPS, and a slight increase in RD from 93.8% to 94.8% was observed. These results indicate that the optimal amount of LiF needs to be carefully optimized. It is possible that the LiF amount used was excessive, leading to the formation of pores and cracking, which could explain the lower density of the resulting materials. Additionally, the mixing process may also need further optimization to ensure homogeneity and proper distribution of the LiF in the ZnS matrix.

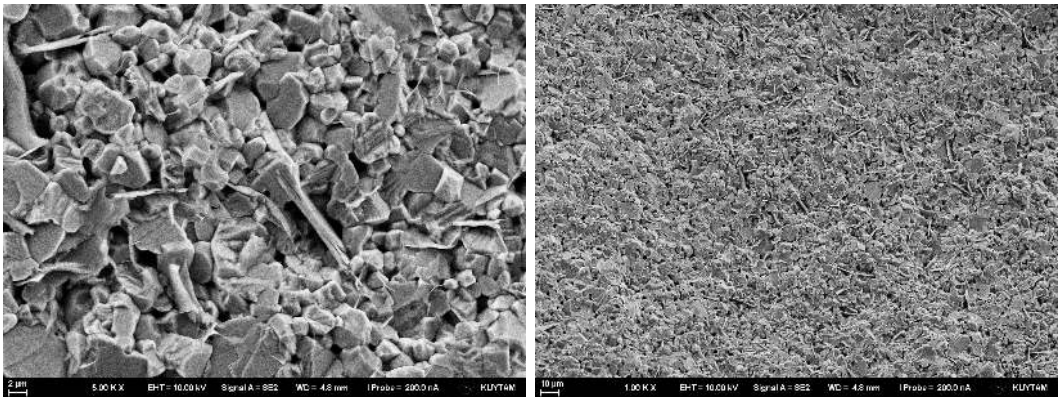

(a) (b)

Figure 6.10: SEM images of the cross section of CPSPS10 coded ZnS ceramics with (a) 2 μm, (b) 10 μm scale bars

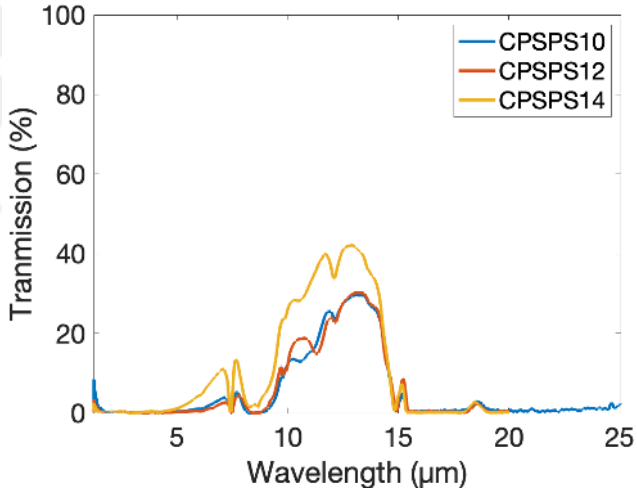

Figure 6.11: Trasmission (%) of CPSPS10 and CPSPS14 samples

Samples X7ABPSPS7 and CPSPS11 were subjected to a hot isostatic pressing (HIP) process for 4 hours at a pressure of 140 MPa at 970 °C, with a heating and cooling rate of 10°C per minute. Following the HIP treatment, there was no significant change observed in the transmission of X7ABPSPS7, while a slight change in transmission was observed for CPSPS11. The post-HIP FTIR results are presented in Figure 6.14. Moreover, scanning electron microscope (SEM) images of the cross sections of the HIPed CPSPS11 and CPSPS10 samples were taken, as shown

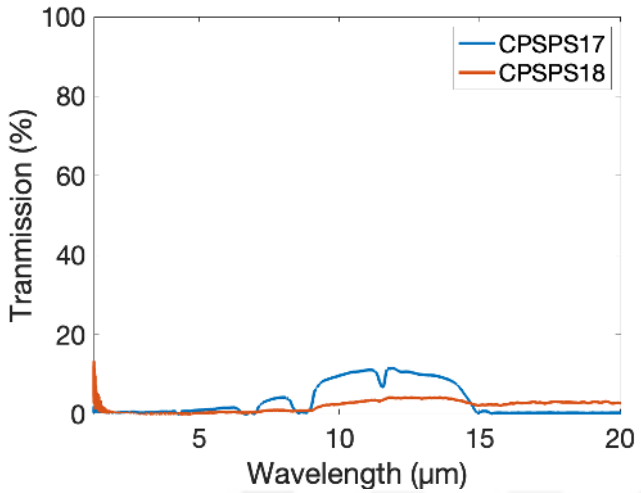

Figure 6.12: Transmission (%) of CPSPS17 and CPSPS18 samples

in Figure 6.10 and Figure 6.15. Although the relative densities of the two samples were similar, their cross-sectional morphologies differed significantly after the HIP process. Notably, there was evident grain growth during HIP, and the grains were clearly visible. Additionally, there were fewer pores in the sample that underwent HIP treatment, indicating improved densification. Further analysis through energy-dispersive X-ray spectroscopy (EDX) revealed the presence of chlorine in the flakes observed in the SEM images of the cross section of the CPSPS10 sample. This suggests the incorporation of chlorine during the synthesis process or a potential source of contamination.

Sample CPSPS10 was subjected to an etching process using boiling 0.1M H_2SO_4 for a duration of 30 seconds. The results of the etching process are depicted in Figure 6.16. Under both unpolarized and polarized light, grains as large as 16 μm were observed and identified. This observation suggests that grain growth occurred during the SPS process. Given that the particles of the commercial powder have a size of only a few microns, the significant increase in grain size indicates the occurrence of grain growth during the fabrication process.

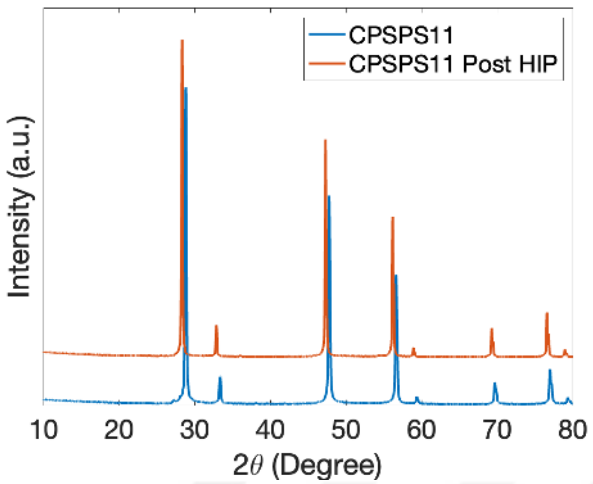

Figure 6.13: XRD pattern of the CPSPS11 sample before and after the HIP

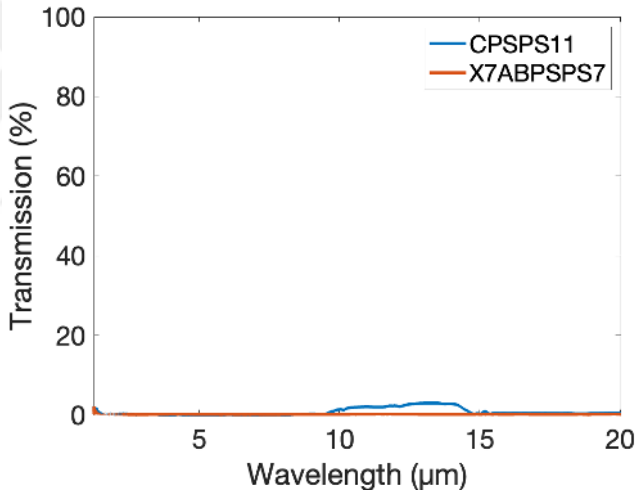

Figure 6.14: Transmission (%) of X7ABPSPS7 and CPSPS11 samples

6.4 Synthesis and Characterization of Bridgman Method

Prior to the synthesis step, the temperature profile of the Bridgman furnace was recorded using a thermocouple at a temperature of 1000°C. This recording aimed to assess the temperature variation and gain insights into the temperature gradient within the furnace. The temperature profile is depicted in Figure 6.17, revealing temperature differences as large as 80°C compared to the set temperature. Additionally, a nearly 20 cm region of constant temperature is observed.

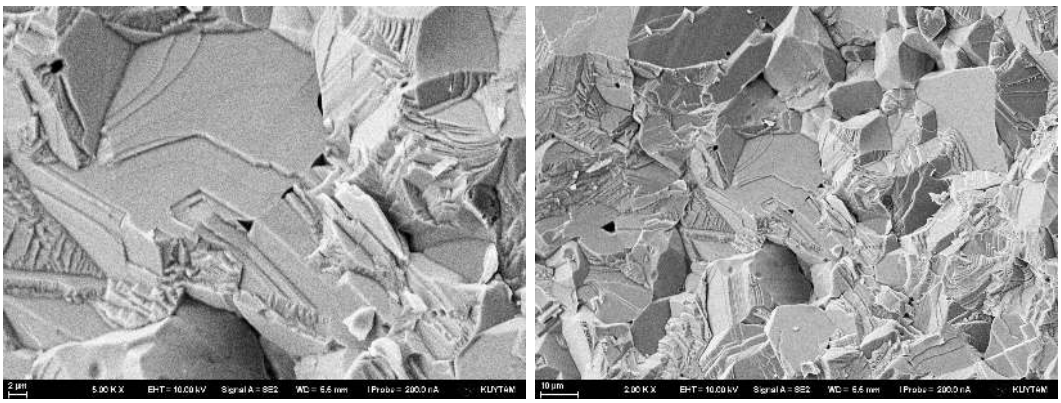

(a) (b)

Figure 6.15: SEM images of the cross section of CPSPS11 coded ZnS ceramics with (a) 2 μm, (b) 10 μm scale bars

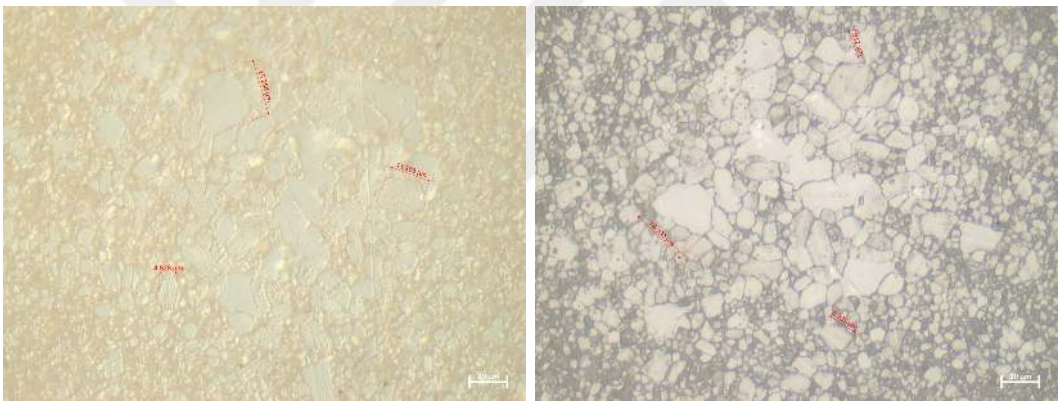

(a) (b)

Figure 6.16: Optical microscopy images of the etched CPSPS10 sample under (a) unpolarized light (b) polarized light

In the experiment for single crystal growth, 1 gram of ZnSe powder (X5) synthesized using the solid-state reaction method was utilized. The XRD pattern of the powder, displaying only the presence of the cubic phase, is presented in Figure 6.19. SEM images of the powder can be observed in Figure 6.18. The powder exhibited sharper features and a greater number of particles with larger sizes in comparison to the ball-milled powders. By employing the Scherrer Equation (5.1), the average

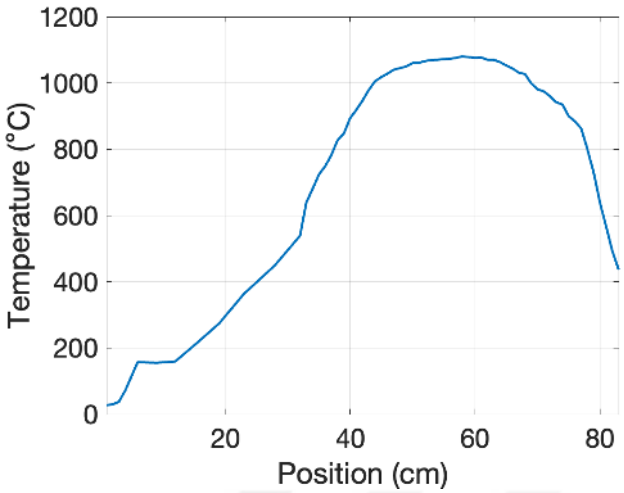

Figure 6.17: The temperature profile of the Bridgman furnace

(a) (b) (c)

Figure 6.18: SEM images of X5 coded ZnSe powder with (a) 200 nm, (b) 1 μm (c) 100 μm scale bars

crystallite size was determined to be 71 nm. The preparation procedure involved placing the cold-pressed powder into an alumina crucible, which was then inserted into a niobium ampoule. All loading processes were performed under an argon atmosphere within a glovebox. Subsequently, the ampoule was positioned in the Bridgman furnace. The furnace was gradually heated to 1550 °C, slightly above the melting temperature. After maintaining this temperature for 3 hours, the melt was gradually lowered at a rate of 2 mm/hour over the course of one week. Throughout the melting and lowering process, a constant flow of argon was maintained inside the furnace.

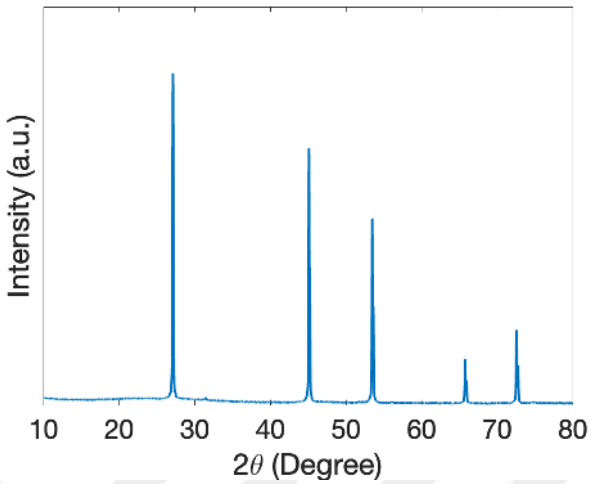

Figure 6.19: XRD pattern of the purified powder synthesized with the solid-state reaction

The solidified material was subsequently collected and subjected to imaging, as displayed in Figure 6.20. Upon visual inspection, multiple single crystal sites were

(a) (b)

Figure 6.20: Images of the syntehesized ZnSe, X8 Sample (a) in daylight (b) under white light

observed, exhibiting slight variations in color. To investigate the underlying causes of this color difference, SEM images were captured for the red and orange crystal sites, presented in Figures 6.22 and 6.21, respectively. The surfaces of the crystals

were predominantly free from cracks or contaminants, although a few cracks with sizes up to 1 μm were noticeable.

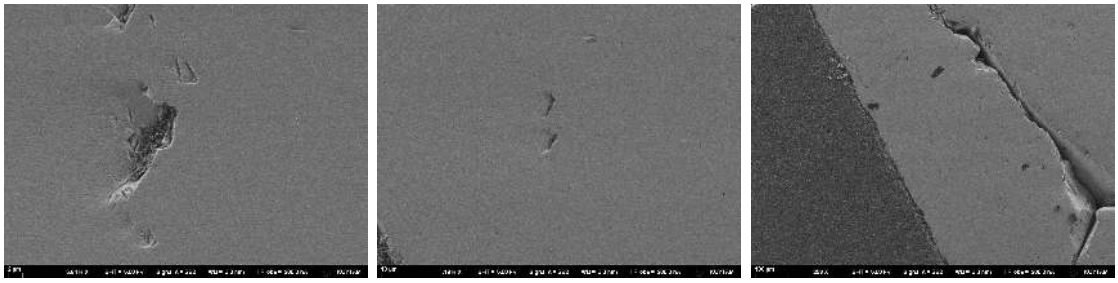

(a) (b) (c)

Figure 6.21: SEM images of X8 coded ZnSe crystals orange part with (a) 2 μm, (b) 10 μm (c) 100 μm scale bars

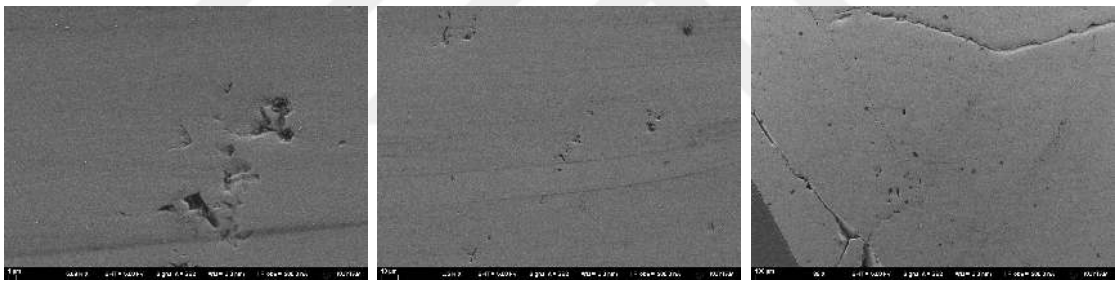

(a) (b) (c)

Figure 6.22: SEM images of X8 coded ZnSe crystals red part with (a) 2 μm, (b) 10 μm (c) 100 μm scale bars

To further analyze these regions with different colors, EDX mappings were performed, as depicted in Figure 6.23. It can be observed in Figure 6.23b that the red portions of the crystal exhibited higher Zn content compared to the orange portion shown in Figure 6.23d. This observation aligned with the darker color of the unpurified ball-milled powders, which contained an excess of Zinc.

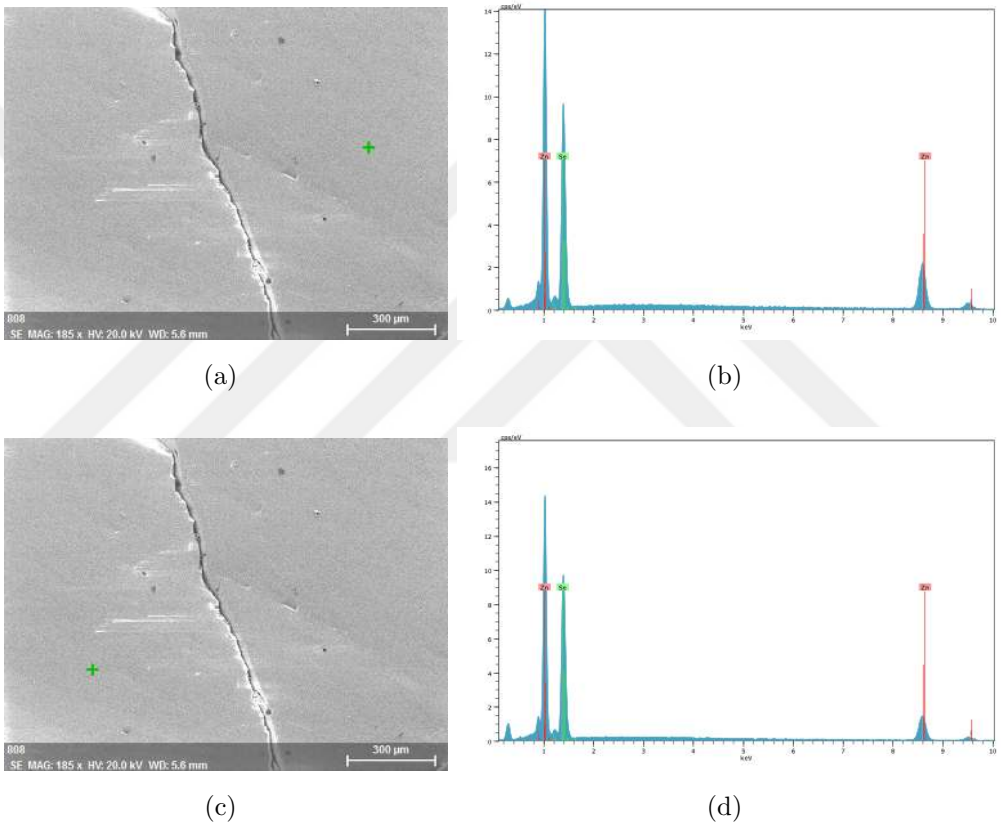

(a) (b)

(c) (d)

Figure 6.23: SEM images of the points (a),(c) where EDX analysis are done and EDX results (b), (d) for the red and orange portions of the X8, respectively.

Chapter 7

CONCLUSION

In conclusion, this thesis presents several significant findings. Firstly, we report the successful implementation of self-Q-switched (SQS) operation in a Tm^{3+}:Lu_2O_3 ceramic laser operating near 2 μm, a novel achievement in this field. The SQS regime resulted in the generation of 9.7 μs pulses at a wavelength of 2091 nm, with a pulse repetition rate of 26 kHz. To enable low-threshold continuous-wave (CW) operation, a carefully designed resonator with tight focusing was utilized, achieving impressive results with lasing threshold pump powers as low as 33 mW. With an incident pump power of 590 mW at 776 nm, the laser achieved a maximum output power of 164 mW at 2097 nm using the double end-pumped configuration, exhibiting a slope efficiency of 30% with respect to the incident pump power. Furthermore, we demonstrated the extended wavelength operation of the laser up to 2235 nm, and anticipate that even higher wavelength operation could be achievable with increased pump powers. Additionally, we successfully synthesized highly pure ZnSe powders using high-energy ball milling and investigated the process of thulium doping. Crystal growth experiments employing the CVT and Bridgman methods resulted in the production of large crystals for ZnS and ZnSe, respectively. Notably, the CVT-grown ZnS sample exhibited a transmission of 40% for a 1.8 mm thick sample. The SEM images of the surfaces and cross-sections of the SPSed samples provided valuable insights into the densification process during SPS and the challenges encountered in achieving transparent ceramics using this method.

For future work, the investigation of doping in Tm:ZnS and Tm:ZnSe materials will be further enhanced by utilizing X-ray Photoelectron Spectroscopy (XPS) and X-ray Fluorescence (XRF) measurements. These techniques will help assess the success and accuracy of the doping process. Moreover, the photoluminescence (PL)

spectrum will be collected at lower wavelengths, allowing for a more comprehensive characterization of the materials' optical properties. Following the optimization of Thulium doping, the synthesis of transparent doped bulk materials will be pursued. The goal is to develop high-quality, optically transparent Tm:ZnS and Tm:ZnSe bulk materials with excellent optical properties. These transparent materials will be essential for applications requiring high transmittance in the MWIR region. In addition to bulk materials, the potential of random lasing in Tm:ZnSe and Tm:ZnS powders will be explored. Random lasers are a fascinating field of study that can provide unconventional lasing behavior, and investigating their occurrence in Tm-doped powders will offer new insights into the properties and potential applications of these materials.

BIBLIOGRAPHY

[Ahamed et al., 2016] Ahamed, A. J., Ramar, K., and Kumar, P. V. (2016). Synthesis and characterization of znse nanoparticles by co-precipitation method. *Journal of nanoscience and technology*, pages 148–150.

[Ahn et al., 2018] Ahn, H.-Y., Choi, W. J., Lee, S. Y., Ju, B.-K., and Cho, S.-H. (2018). Mechanochemical synthesis of zns for fabrication of transparent ceramics. *Research on Chemical Intermediates*, 44:4721–4731.

[Anila et al., 2015] Anila, E., Safeera, T., and Reshmi, R. (2015). Photoluminescence of nanocrystalline zns thin film grown by sol–gel method. *Journal of Fluorescence*, 25:227–230.

[Antipov et al., 2016] Antipov, O., Novikov, A., Larin, S., and Obronov, I. (2016). Highly efficient 2 μm cw and q-switched Tm^{3+}:Lu_2O_3 ceramics lasers in-band pumped by a raman-shifted erbium fiber laser at 1670 nm. *Optics Letters*, 41(10):2298–2301.

[Antipov et al., 2015] Antipov, O. L., Eranov, I. D., Frolov, M. P., Korostelin, Y. V., Kozlovsky, V. I., Novikov, A. A., Podmarkov, Y. P., and Skasyrsky, Y. K. (2015). 2.92 μm $Cr^{2+} : CdSe$ single crystal laser pumped by a repetitively pulsed Tm^{3+}:Lu_2O_3 ceramics laser at 2.066 μm. *Laser Physics Letters*, 12(4):045801.

[Antipov et al., 2021] Antipov, O. L., Getmanovskiy, Y. A., Balabanov, S. S., Larin, S. V., and Sharkov, V. V. (2021). 1940 nm, 1966 nm and 2066 nm multi-wavelength cw and passively-q-switched operation of l-shaped Tm^{3+}:Lu_2O_3 ceramic laser in-band fiber-laser pumped at 1670 nm. *Laser Physics Letters*, 18(5):6.

[Antipov et al., 2011] Antipov, O. L., Golovkin, S. Y., Gorshkov, O. N., Zakharov, N. G., Zinov'ev, A. P., Kasatkin, A. P., Kruglova, M. V., Marychev, M. O.,

Novikov, A. A., Sakharov, N. V., and Chuprunov, E. V. (2011). Structural, optical, and spectroscopic properties and efficient two-micron lasing of new Tm^{3+}:Lu_2O_3 ceramics. *Quantum Electronics*, 41(10):863–868.

[Antipov et al., 2012] Antipov, O. L., Novikov, A. A., Zakharov, N. G., and Zinoviev, A. P. (2012). Optical properties and efficient laser oscillation at 2066 nm of novel Tm^{3+}:Lu_2O_3 ceramics. *Optical Materials Express*, 2(2):183–189.

[Avetisov et al., 2018] Avetisov, R., Balabanov, S., Firsov, K., Gavrishchuk, E., Gladilin, A., Ikonnikov, V., Kalinushkin, V., Kazantsev, S. Y., Kononov, I., Zykova, M., et al. (2018). Hot-pressed production and laser properties of znse: Fe2+. *Journal of Crystal Growth*, 491:36–41.

[Baylam et al., 2018] Baylam, I., Ozharar, S., and Sennaroglu, A. (2018). 1200 nm pumped Tm^{3+}:Lu_2O_3 ceramic lasers. *Appl Opt*, 57(8):1772–1776.

[Belyaev et al., 2016] Belyaev, A. N., Chabushkin, A. N., Khrushchalina, S. A., Kuznetsova, O. A., Lyapin, A. A., Romanov, K. N., and Ryabochkina, P. A. (2016). Investigation of endovenous laser ablation of varicose veins in vitro using 1.885-μm laser radiation. *Lasers in Medical Science*, 31(3):503–510.

[Beyatli et al., 2013] Beyatli, E., Sennaroglu, A., and Demirbas, U. (2013). Self-q-switched $Cr : LICAF$ laser. *Journal of the Optical Society of America B-Optical Physics*, 30(4):914–921.

[Beyatlı et al., 2020] Beyatlı, E., Kaya, F., and Bilici, H. (2020). Self-q-switched and multicolor operation of a $Tm : LuAG$ laser. *Applied Optics*, 59(27):8247–8252.

[Cai et al., 2015] Cai, W., Liu, J., Li, C., Zhu, H. T., Ge, P. G., Zheng, L. H., Su, L. B., and Xu, J. (2015). Compact self-q-switched laser near 2 μm. *Optics Communications*, 334:287–289.

[Canbaz et al., 2017] Canbaz, F., Yorulmaz, I., and Sennaroglu, A. (2017). Kerr-lens mode-locked 2.3-μm $Tm^{3+} : YLF$: laser as a source of femtosecond pulses in the mid-infrared. *Opt Lett*, 42(19):3964–3967.

[Chen et al., 2015] Chen, Y., Zhang, L., Zhang, J., Liu, P., Zhou, T., Zhang, H., Gong, D., Tang, D., and Shen, D. (2015). Fabrication of transparent zns ceramic by optimizing the heating rate in spark plasma sintering process. *Optical Materials*, 50:36–39.

[Chlique et al., 2011] Chlique, C., Delaizir, G., Merdrignac-Conanec, O., Roucau, C., Dollé, M., Rozier, P., Bouquet, V., and Zhang, X. (2011). A comparative study of zns powders sintering by hot uniaxial pressing (hup) and spark plasma sintering (sps). *Optical Materials*, 33(5):706–712.

[Dong et al., 2002] Dong, J., Deng, P. Z., and Bass, M. (2002). $Cr, Nd : YAG$ self-q-switched laser with high efficiency output. *Optics and Laser Technology*, 34(7):589–594.

[Eremeev et al., 2022] Eremeev, K., Loiko, P., Braud, A., Camy, P., Zhang, J., Xu, X., Zhao, Y., Liu, P., Balabanov, S., Dunina, E., Kornienko, A., Fomicheva, L., Mateos, X., Griebner, U., Petrov, V., Wang, L., and Chen, W. (2022). Spectroscopy of solid-solution transparent sesquioxide laser ceramic $Tm : LuYO_3$. *Optical Materials Express*, 12(9):3749–3762.

[Faraji et al., 2018] Faraji, G., Kim, H. S., and Kashi, H. T. (2018). Introduction. In Faraji, G., Kim, H. S., and Kashi, H. T., editors, *Severe Plastic Deformation*, pages 1–17. Elsevier.

[Fedin et al., 2001] Fedin, A. V., Kyalbieva, S. A., Gavrilov, A. V., and Smetanin, S. N. (2001). Self-q-switching at phase conjugation in active media. In *7th International Conference on Laser and Laser-Information Technologies*, volume 4644 of *Proceedings of SPIE*, pages 312–318, BELLINGHAM. Spie-Int Soc Optical Engineering.

[Firsov et al., 2015] Firsov, K., Gavrishchuk, E., Ikonnikov, V., Kazantsev, S. Y., Kononov, I., Rodin, S., Savin, D., and Timofeeva, N. (2015). High-energy room-temperature fe2+: Zns laser. *Laser Physics Letters*, 13(1):015001.

[Frage et al., 2012] Frage, N., Kalabukhov, S., Sverdlov, N., Kasiyan, V., Rothman, A., and Dariel, M. (2012). Effect of the spark plasma sintering (sps) parameters and lif doping on the mechanical properties and the transparency of polycrystalline nd-yag. *Ceramics International*, 38(7):5513–5519.

[Frolov et al., 2013] Frolov, M., Korostelin, Y. V., Kozlovsky, V., Mislavskii, V., Podmar'kov, Y. P., Savinova, S., and Skasyrsky, Y. K. (2013). Study of a 2-j pulsed fe: Znse 4-μm laser. *Laser Physics Letters*, 10(12):125001.

[Furuse et al., 2018] Furuse, H., Nakasawa, S., Yoshida, H., Morita, K., Suzuki, T. S., Kim, B.-N., Sakka, Y., and Hiraga, K. (2018). Transparent ultrafine yb3+: Y2o3 laser ceramics fabricated by spark plasma sintering. *Journal of the American Ceramic Society*, 101(2):694–702.

[Gao et al., 2021] Gao, M., Yang, H., Shen, H., Zeng, Z., Fan, F., Tang, B., Min, J., Zhang, Y., Hua, Q., Li, L. S., et al. (2021). Bulk-like znse quantum dots enabling efficient ultranarrow blue light-emitting diodes. *Nano Letters*, 21(17):7252–7260.

[Guillemot et al., 2019] Guillemot, L., Loiko, P., Braud, A., Doualan, J. L., Hideur, A., Koselja, M., Moncorge, R., and Camy, P. (2019). Continuous-wave $Tm : YAlO_3$ laser at approximately 2.3 μm. *Opt Lett*, 44(20):5077–5080.

[He et al., 2022] He, J. R., Song, R., Jiang, L., and Hou, J. (2022). Ultra-compact 50 w flat supercontinuum generation in single-stage self-q-switched fiber laser with photonic crystal fiber. *Ieee Photonics Journal*, 14(2):6.

[Hoa et al., 2009] Hoa, T. T. Q., Canh, T. D., Long, N. N., et al. (2009). Preparation of zns nanoparticles by hydrothermal method. In *Journal of Physics: Conference Series*, volume 187, page 012081. IOP Publishing.

[Hwang et al., 2005] Hwang, J.-m., Oh, M.-O., Kim, I., Lee, J.-K., and Ha, C.-S. (2005). Preparation and characterization of zns based nano-crystalline particles for polymer light-emitting diodes. *Current Applied Physics*, 5(1):31–34.

[Iranmanesh et al., 2015] Iranmanesh, P., Saeednia, S., and Nourzpoor, M. (2015). Characterization of zns nanoparticles synthesized by co-precipitation method. *Chinese Physics B*, 24(4):046104.

[Ivakin et al., 2013] Ivakin, E. V., Kisialiou, I. G., and Antipov, O. L. (2013). Laser ceramics Tm^{3+}:Lu_2O_3. thermal, thermo-optical, and spectroscopic properties. *Optical Materials*, 35(3):499–503.

[Jørgensen et al., 2008] Jørgensen, J.-E., Jensen, T., and Hanson, J. (2008). Hydrothermal synthesis of nanocrystalline znse: An in situ synchrotron radiation x-ray powder diffraction study. *Journal of Solid State Chemistry*, 181(8):1925–1929.

[Kang et al., 2022] Kang, P. Q., Zhang, S., Zhang, X. L., and Huang, J. J. (2022). High power self-q-switched $Tm : YAP$ solid state laser based on the ground state reabsorption. *Infrared Physics & Technology*, 123:7.

[Khaled et al., 2021] Khaled, J., Sato, T., Koide, M., and Sato, H. (2021). Development of near-net dome shaped zns window for the infrared region using spark plasma sintering technique. In *Infrared Imaging Systems: Design, Analysis, Modeling, and Testing XXXII*, volume 11740, pages 184–196. SPIE.

[Kim et al., 2008] Kim, G.-S., Shin, D. H., Seo, Y. I., and Do Kim, Y. (2008). Microstructure and mechanical properties of a zns–sio2 composite prepared by ball-milling and spark plasma sintering. *Materials characterization*, 59(9):1201–1205.

[Kolker et al., 2019] Kolker, D. B., Antipov, O. L., Larin, S. V., Isaenko, L. I., Vedenyapin, V. N., Ahmatkhanov, A. R., and Shur, V. Y. (2019). Mid-ir

optical parametric oscillator based on periodically polled $LiNbO_3$ pumped by Tm^{3+}:Lu_2O_3 ceramic laser. *Atmospheric and Oceanic Optics*, 32(6):724–729.

[Komar et al., 2009] Komar, V., Nalivaiko, D., Sulima, S., Zagoruiko, Y. A., Fedorenko, O., Kovalenko, N., Chugai, O., Terzin, I., Gerasimenko, A., and Dubina, N. (2009). Znse: Cr^{2+} laser crystals grown by bridgman method. *Functional materials*.

[Koopmann et al., 2011a] Koopmann, P., Lamrini, S., Scholle, K., Fuhrberg, P., Petermann, K., and Huber, G. (2011a). Efficient diode-pumped laser operation of Tm^{3+}:Lu_2O_3 around 2 μm. *Optics Letters*, 36(6):948–950.

[Koopmann et al., 2011b] Koopmann, P., Peters, R., Petermann, K., and Huber, G. (2011b). Crystal growth, spectroscopy, and highly efficient laser operation of thulium-doped Lu_2O_3 around 2 μm. *Applied Physics B*, 102(1):19–24.

[Krause et al., 1994] Krause, E., Hartmann, H., Menninger, J., Hoffmann, A., Fricke, C., Heitz, R., Lummer, B., Kutzer, V., and Broser, I. (1994). Influence of growth non-stoichiometry on optical properties of doped and non-doped znse grown by chemical vapour deposition. *Journal of crystal growth*, 138(1-4):75–80.

[Lagatsky et al., 2013] Lagatsky, A. A., Sun, Z., Kulmala, T. S., Sundaram, R. S., Milana, S., Torrisi, F., Antipov, O. L., Lee, Y., Ahn, J. H., Brown, C. T. A., Sibbett, W., and Ferrari, A. C. (2013). 2μm solid-state laser mode-locked by single-layer graphene. *Applied Physics Letters*, 102(1):013113.

[Lauck, 2010] Lauck, R. (2010). Chemical vapor transport of zinc sulfide. *Journal of crystal growth*, 312(24):3642–3649.

[Lee et al., 2021] Lee, J.-H., Kim, B.-N., and Jang, B.-K. (2021). Fabrication of transparent y2o3 ceramics by two-step spark plasma sintering. *Journal of the American Ceramic Society*, 104(11):5501–5508.

[Lee et al., 2008] Lee, W. G., Kim, Y. K., Kim, J. K., Starzhinskiy, N., Ryzhikov, V., and Grinyov, B. (2008). Properties of znse: Te, o crystals grown by bridgman-stockbarger method. *Journal of Nuclear Science and Technology*, 45(sup5):579–581.

[Li and Jie, 2003] Li, H. and Jie, W. (2003). Growth and characterizations of bulk znse single crystal by chemical vapor transport. *Journal of Crystal Growth*, 257(1-2):110–115.

[Li et al., 2008] Li, J., Wang, M., Huo, X., Yao, X., et al. (2008). Preparation and optical properties of dispersible znse nanocrystals synthesized by high energy ball milling. *Ceramics international*, 34(4):1077–1080.

[Li et al., 2019] Li, W. S., Wu, J. J., Cai, Z. P., Guan, X. F., and Xu, H. Y. (2019). Directly blue diode-pumped green self-q-switched ho-3-doped fluoride all-fiber laser at similar to 550 nm. *Journal of Lightwave Technology*, 37(22):5727–5732.

[Liu et al., 2016] Liu, J., Fan, X., Liu, J., Ma, W., Wang, J., and Su, L. (2016). Mid-infrared self-q-switched $Er, Pr : CaF_2$ diode-pumped laser. *Optics Letters*, 41(20):4660–4663.

[Liu et al., 2006] Liu, J., Yan, P., Yue, G., Kong, L., Zhuo, R., and Qu, D. (2006). Synthesis of doped zns one-dimensional nanostructures via chemical vapor deposition. *Materials Letters*, 60(29-30):3471–3476.

[Liu et al., 2022] Liu, Z., Toci, G., Pirri, A., Patrizi, B., Feng, Y., Hu, D., Chen, H., Hreniak, D., Vannini, M., and Li, J. (2022). Fabrication and characterizations of Tm^{3+}:Lu_2O_3 transparent ceramics for 2μm laser applications. *Optical Materials*, 131:112705.

[Loiko et al., 2018] Loiko, P., Koopmann, P., Mateos, X., Serres, J. M., Jambunathan, V., Lucianetti, A., Mocek, T., Aguiló, M., Díaz, F., Griebner, U., Petrov, V., and Kränkel, C. (2018). Highly efficient, compact $Tm^{3+} : RE_2O_3$ (re

= y, lu, sc) sesquioxide lasers based on thermal guiding. *IEEE Journal of Selected Topics in Quantum Electronics*, 24(5):1–13.

[Lu et al., 2002] Lu, F. Y., Xu, Z. G., and Wang, H. J. (2002). The study of self-q-switched of asymmetry flat-flat cavity solid laser. In *Conference on High-Power Lasers and Application II*, volume 4914 of *Proceedings of the Society of Photo-Optical Instrumentation Engineers (Spie)*, pages 87–90, BELLINGHAM. Spie-Int Soc Optical Engineering.

[Luo et al., 2021] Luo, Y., Yin, M., Chen, L., Yu, S., and Kang, B. (2021). Hot-pressed fe 2+: Znse ceramics with powders fabricated via grinding chemical vapor deposition znse polycrystalline. *Optical Materials Express*, 11(8):2744–2752.

[McCloy et al., 2011] McCloy, J., Fest, E., Korenstein, R., and Poisl, W. H. (2011). Anisotropy in structural and optical properties of chemical vapor deposited zns. In *Window and Dome Technologies and Materials XII*, volume 8016, pages 166–176. SPIE.

[Mierczyk et al., 2002] Mierczyk, Z., Majchrowski, A., and Kityk, I. V. (2002). Znse: Co 2+ crystals as saturable absorbers for laser applications. In *Proceedings of SPIE*, volume 5136, pages 31–35.

[Morova et al., 2022] Morova, Y., Khan, M., Denker, B., Galagan, B., Sverchkov, S., and Sennaroglu, A. (2022). Tunable continuous-wave laser operation of Tm^{3+} ion doped tellurite glass near 2μm. *Journal of Luminescence*, 252:119318.

[Muti et al., 2019] Muti, A., Tonelli, M., Petrov, V., and Sennaroglu, A. (2019). Continuous-wave mid-infrared laser operation of $Tm^{3+} : KY_3F_10$ at 2.3 μm. *Optics Letters*, 44(13):3242–3245.

[Niu et al., 2021] Niu, Z. Q., Feng, T. L., Li, T., Yang, K. J., Zhao, J., Li, G. Q., Li, D. C., Zhao, S. Z., Qiao, W. C., Chu, H. W., and Liu, Y. Z. (2021). Theoretical and experimental investigations on doubly q-switched $Tm : YAP$ laser with eom and Sb_2Te_3 nanosheets. *Optics Express*, 29(16):24684–24694.

[Noda et al., 1990] Noda, K., Matsumura, N., Otsuka, S., and Matsumoto, K. (1990). Chemical-vapor-transport rate of zns in closed tube. *Journal of The Electrochemical Society*, 137(4):1281.

[Oh et al., 2004] Oh, C., Wang, J., and Isshiki, M. (2004). Vertical bridgman growth and annealing effect of bi doped znse single crystal. *physica status solidi (c)*, 1(10):2495–2499.

[Okereke and Ekpunobi, 2011] Okereke, N. and Ekpunobi, A. (2011). Znse buffer layer deposition for solar cell application. *Journal of Non-oxide glasses*, 3(1):31.

[Oztulum, 2022] Oztulum, S. (2022). Developing transparent polycrystalline zinc selenide (znse) pellets for laser applications. Master's thesis, Koc University.

[Pathak et al., 2013] Pathak, C., Mishra, D., Agarwala, V., and Mandal, M. (2013). Optical properties of zns nanoparticles prepared by high energy ball milling. *Materials science in semiconductor processing*, 16(2):525–529.

[Pirri et al., 2022] Pirri, A., Maksimov, R. N., Li, J., Vannini, M., and Toci, G. (2022). Achievements and future perspectives of the trivalent thulium-ion-doped mixed-sesquioxide ceramics for laser applications. *Materials*, 15(6).

[Pol et al., 2008] Pol, S. V., Pol, V. G., Calderon-Moreno, J. M., Cheylan, S., and Gedanken, A. (2008). Facile synthesis of photoluminescent zns and znse nanopowders. *Langmuir*, 24(18):10462–10466.

[Razdobreev and Shestakov, 2006] Razdobreev, I. and Shestakov, A. (2006). Self-pulsing of a monolithic tm-doped $YAlO_3$ microlaser. *Physical Review A*, 73(5).

[Ryzhikov et al., 2001] Ryzhikov, V., Starzhinskiy, N., Gal'Chinetskii, L., Gashin, P., Kozin, D., and Danshin, E. (2001). New semiconductor scintillators znse (te, o) and integrated radiation detectors based thereon. *IEEE Transactions on Nuclear Science*, 48(3):356–359.

[Sakajio et al., 2022] Sakajio, M., Beilin, V., Mann-Lahav, M., Zamir, S., Shter, G. E., and Grader, G. S. (2022). Highly transparent polycrystalline mgo via spark plasma sintering. *ACS Applied Materials & Interfaces*, 14(46):52108–52116.

[Schmidt et al., 2012] Schmidt, A., Koopmann, P., Huber, G., Fuhrberg, P., Choi, S. Y., Yeom, D. I., Rotermund, F., Petrov, V., and Griebner, U. (2012). 175 fs Tm^{3+}:Lu_2O_3 laser at 2.07 μm mode-locked using single-walled carbon nanotubes. *Optics Express*, 20(5):5313–5318.

[Sennaroglu, 2010] Sennaroglu, A. (2010). *Photonics and Laser Engineering: Principles, Devices, and Applications*. McGraw-Hill Education.

[Sennaroglu, 2019] Sennaroglu, A. (2019). Classification of power-degrading mechanisms in an optically pumped four-level laser: an analytical approach. *JOSA B*, 36(8):2202–2209.

[Singh et al., 2015] Singh, U. N., Walsh, B. M., Yu, J., Petros, M., Kavaya, M. J., Refaat, T. F., and Barnes, N. P. (2015). Twenty years of $Tm : Ho : YLF$ and $LuLiF$ laser development for global wind and carbon dioxide active remote sensing. *Optical Materials Express*, 5(4):827–837.

[Sorokina et al., 2002] Sorokina, I. T., Sorokin, E., Mirov, S., Fedorov, V., Badikov, V., Panyutin, V., Di Lieto, A., and Tonelli, M. (2002). Continuous-wave tunable cr2+: Zns laser. *Applied Physics B*, 74:607–611.

[Sun et al., 2021] Sun, J. J., Chen, Y., Zhang, K., Pan, Q. K., He, Y., Yu, D. Y., and Chen, F. (2021). Efficient continuous wave and acousto-optical q-switched Tm^{3+}:Lu_2O_3 laser pumped by the laser diode at 1.7 μm. *Infrared Physics & Technology*, 116:4.

[Suzuki et al., 2021] Suzuki, A., Krankel, C., and Tokurakawa, M. (2021). Sub-6 optical-cycle kerr-lens mode-locked Tm^{3+}:Lu_2O_3 and Tm^{3+}:Sc_2O_3 combined gain media laser at 2.1 μm. *Optics Express*, 29(13):19465–19471.

[Velumani and Ascencio, 2004] Velumani, S. and Ascencio, J. (2004). Formation of zns nanorods by simple evaporation technique. *Applied Physics A*, 79:153–156.

[Vetrovec et al., 2018] Vetrovec, J., Filgas, D. M., Smith, C. A., Copeland, D. A., Litt, A. S., Briscoe, E., and Schirmer, E. (2018). 2-micron lasing in Tm^{3+}:Lu_2O_3 ceramic: Initial operation. In *Conference on Solid State Lasers XXVII - Technology and Devices*, volume 10511 of *Proceedings of SPIE*, BELLINGHAM. Spie-Int Soc Optical Engineering.

[Voronov et al., 2008] Voronov, A. A., Kozlovskii, V. I., Korostelin, Y. V., Landman, A. I., Podmar'Kov, Y. P., Skasyrskii, Y. K., and Frolov, M. P. (2008). A continuous-wave fe2+: Znse laser. *Quantum Electronics*, 38(12):1113.

[Wang et al., 2001] Wang, J., Omino, A., and Isshiki, M. (2001). Growth and conductive type control of znse single crystals by vertical bridgman method. *Journal of crystal growth*, 229(1-4):69–73.

[Wang et al., 2022] Wang, S. X., Liu, H. L., Mu, W. X., Ren, Y. Y., Jia, Z. T., Fu, X. W., Sun, X. L., and Jia, Y. C. (2022). Dual-wavelength self-q-switched mode-locked waveguide lasers based on $Nd : LGGG$ cladding waveguides. *Optical Materials Express*, 12(3):854–862.

[Wang et al., 2012] Wang, X., Xie, Z., Huang, H., Liu, Z., Chen, D., and Shen, G. (2012). Gas sensors, thermistor and photodetector based on zns nanowires. *Journal of Materials Chemistry*, 22(14):6845–6850.

[Wei et al., 2017] Wei, S., Zhang, L., Yang, H., Zhou, T., Wong, C., Zhang, Q., and Chen, H. (2017). Preliminary study of 3d ball-milled powder processing and sps-accelerated densification of znse ceramics. *Optical Materials Express*, 7(4):1131–1140.

[Wherrett, 1991] Wherrett, B. (1991). Znse switching and logic devices and their application to information processing. *Semiconductor Science and Technology*, 6(9A):A65.

[Wu et al., 2015] Wu, K. S., Henderson-Sapir, O., Veitch, P. J., Hamilton, M., Munch, J., and Ottaway, D. J. (2015). Self-pulsing in tm-doped $yalo_3$ lasers: Excited-state absorption and chaos. *Physical Review A*, 91(4):043819.

[Wu et al., 1989] Wu, P., Kershaw, R., Dwight, K., and Wold, A. (1989). Growth and characterization of nickel-doped zns single crystals. *Materials research bulletin*, 24(1):49–53.

[Zhang et al., 2018] Zhang, B., Li, L., He, C. J., Tian, F. J., Yang, X. T., Cui, J. H., Zhang, J. Z., and Sun, W. M. (2018). Compact self-q-switched $Tm : YLF$ laser at 1.91 μm. *Optics and Laser Technology*, 100:103–108.

[Zhang et al., 2020a] Zhang, W., Bai, H. L., Guo, L. P., and Li, M. X. (2020a). Self-q-switched operation in $Tm : YAG$ crystal and passively q-switched operation using $GaSe$ saturable absorber. *Infrared Physics & Technology*, 105:4.

[Zhang et al., 2020b] Zhang, W., Ding, S., Zhuang, W., Wu, D., Liu, P., Qu, X., Liu, H., Yang, H., Wu, Z., Wang, K., et al. (2020b). Inp/zns/zns core/shell blue quantum dots for efficient light-emitting diodes. *Advanced Functional Materials*, 30(49):2005303.

[Zhang et al., 2021] Zhang, W. S., Li, L. J., Zhou, S., and Gao, Q. (2021). High-efficiency diode-resonantly-pumped Tm^{3+}:Lu_2O_3 ceramic laser with near diffraction-limited beam quality. *Journal of Russian Laser Research*, 42(3):358–362.

[Zhang et al., 2022] Zhang, W. Y., Tong, L. Y., Yuan, Y., Chen, C., Cai, Y., and Zhao, L. (2022). Self-q-switched $Tm : YAP$ vortex laser by thermal-lensing effect. *Infrared Physics & Technology*, 123:5.

[Zu et al., 2020] Zu, Y. Q., Zong, M. Y., Wang, Y. X., Zhang, Z., Zhang, Z. H., Wu, A. H., Liu, J., and Su, L. B. (2020). Self-q-switched and broad wavelength-tunable lasing in Tm^{3+}-doped CaF_2 single-crystal fiber. *Applied Physics Express*, 13(10):5.